# Experimental and Computational Studies of Turbulent Mass Transfer in a Mixing Channel

Lene K. Hjertager Osenbroch[*]        Bjorn H. Hjertager[†]

Tron Solberg[‡]

[*]Aalborg University Esbjerg, lene.osenbroch@lyse.net

[†]University of Stavanger, bjorn.hjertager@uis.no

[‡]Aalborg University Esbjerg, tron@aaue.dk

# Experimental and Computational Studies of Turbulent Mass Transfer in a Mixing Channel[*]

Lene K. Hjertager Osenbroch, Bjorn H. Hjertager, and Tron Solberg

## Abstract

Experiments are carried out for passive mixing in order to obtain local mean and turbulent velocities and concentrations. The mixing takes place in a square channel with two inlets separated by a block. A combined PIV/PLIF technique is used to obtain instantaneous velocity and concentration fields. Three different flow cases are studied. The 2D numerical predictions of the mixing channel show that none of the $k$ - $\epsilon$ turbulence models tested is suitable for the flow cases studied here. The turbulent Schmidt number is reduced to obtain a better agreement between the measured and predicted mean and fluctuating concentrations. The multi-peak presumed PDF mixing model is tested and comparisons with experiments are encouraging.

**KEYWORDS:** mixing, PIV, PLIF, CFD, mass transfer, probability density function

---

# 1. INTRODUCTION

## 1.1 Statement of problem

Turbulent mass transfer in liquid flows is involved in many processes in the chemical process industry. Turbulence has the ability to mix and transport species, momentum and energy much faster than is done by molecular diffusion and is therefore employed in e.g. chemical reactors to make them perform better. It is of great importance to have a detailed understanding of the turbulent mixing process when developing and validating numerical models to describe the phenomena. Only experimental verification of turbulent mixing will be able to give this insight. The mixing process can be described as turbulent transport of mass by turbulent velocity fluctuations. Experimental study of turbulent mixing thereby requires simultaneous measurement of the instantaneous velocity and concentration fields. Combining Particle Image Velocimetry (PIV) and Planar Laser Induced Fluorescence (PLIF) makes this type of measurement possible.

## 1.2 Previous work

Over the last few years, several successful applications of the combined PIV/PLIF have been documented in the literature. Aanen et al. (1999) developed a combined measurement technique in which PIV and LIF were used simultaneously, without influencing each other. The reliability and precision of the technique was tested by measuring the mixing of a point source placed in the centre of a fully developed turbulent pipe flow. The experimental results were compared against results of a direct numerical simulation (DNS) and against analytical results. The agreement was found to be satisfactory.

Fukushima et al. (2000) studied mixing of a passive scalar in a self-preserving axis-symmetric jet at a Reynolds number of 2000 by using the combined PIV/PLIF technique. The experimental results agreed well with results from DNS and previous experimental data.

Law and Wang (2000) developed a combined PIV and PLIF set-up and demonstrated that the combined set-up can be used to successfully capture the mean and turbulent mass transport characteristics in a mixing process. The combined set-up was applied to a turbulent jet discharging into a stagnant environment. They compared the various mass transport quantities measured to already existing experimental data. The comparisons were mostly found to be satisfactory.

Tsai et al. (1999) developed a simultaneous PIV/Reactive PLIF system. The system was applied to measure velocity and reacting species concentration in

a mixing layer. The measurement results were compared to CFD simulations. The CFD predictions of mean concentration were found to be satisfactory.

Borg et al. (2001) developed a simultaneous PIV/PLIF technique and applied the technique to measure concentration and velocity in the near inlet region of a turbulent jet. The measurements were compared with large eddy simulations (LES) and earlier experimental data. The agreement was generally found to be good.

Meyer et al. (2000) also performed measurements with PLIF combined with PIV. The mixing of a jet in a fully developed cross-flow in a square duct was considered. The experimental results were compared with measurements conducted in the same set-up using point-wise LIF and LDA. The two techniques were in general found to give results in good agreement with each other.

Feng et al. (2005) did PIV/PLIF measurements and CFD analysis of a confined mixing layer. Computational fluid dynamics (CFD) models, including a two-layer $k - \varepsilon$ turbulence model, gradient-diffusion model, and a scalar dissipation rate model, were validated against the experimental data. The experimental and computational results were found to be in good agreement.

The present authors have also reported both measurements of passive mixing (Hjertager et al., 2003) as well as measurements and predictions of a reacting species (Hjertager Osenbroch et al., 2005) in a mixing channel. These works are part of a comprehensive experimental and computational study to be presented in this paper.

## 1.3 Objectives of present work

In this work, the combined PIV and PLIF technique is used to measure turbulent mixing in a confined wake flow. Measurements are performed in the initial mixing zone and also further out in the channel. Validation of the $k - \varepsilon$ turbulence model and different modifications of this model against the experimental data will be done. The so-called multi-peak presumed PDF mixing model will also be investigated (Fox, 1998).

## 2. EXPERIMENTAL TECHNIQUE AND SETUP

### 2.1 Experimental setup

The combined PIV and PLIF technique is used for the measurements. PIV is used to measure the instantaneous velocity field and PLIF is used to measure the instantaneous concentrations. A schematic drawing of the experimental setup including the PIV/PLIF system is shown in Figure 1.
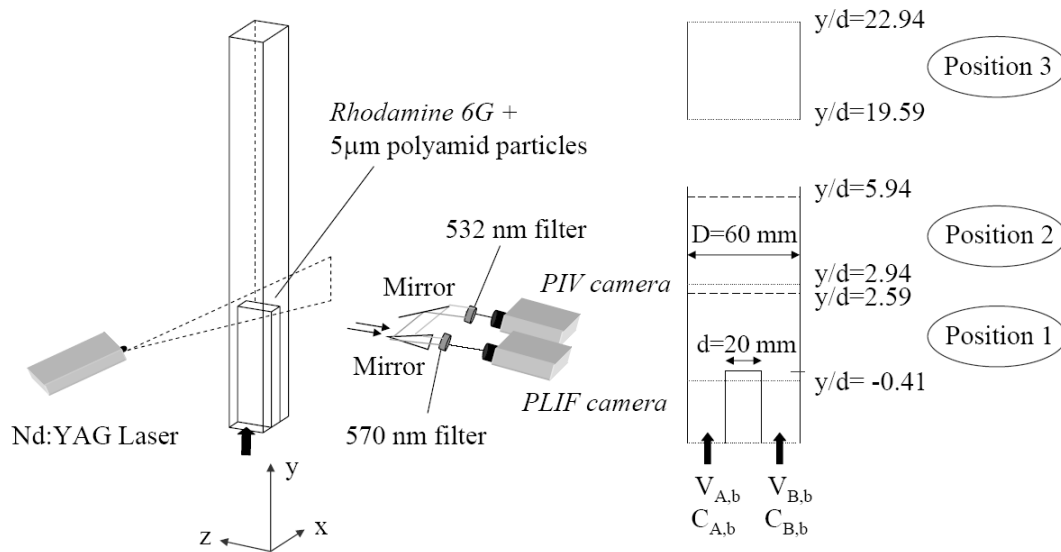
**Figure 1.** A schematic drawing of the experimental set-up including the PIV/PLIF system (left) and the measurement positions (right).

The measurements are performed in a mixing channel with a cross section of $60 \times 60$ mm$^2$. The first part of the channel is divided into two smaller feed channels with a cross section of $20 \times 60$ mm$^2$ by an obstruction of size $20 \times 60 \times 330$ mm$^3$. This is done to allow mixing of the two streams in the main channel. The fluid used is tap water at room temperature.

The flow enters the feed channels from a feed chamber, which is divided by an obstruction with the same thickness as the obstruction in the feed channels. To get a smooth transition of the flow from the feed chambers, it is fitted with a contraction. Preliminary measurements showed that this is not enough to straighten out the flow, therefore flow straighteners are put into the first part of the feed channels. The channel has a total length of 970 mm, and the length available for mixing is 640 mm. The feed solutions are pumped from two large storage tanks each with a volume of 250 L. Both tanks contain water added with 5 μm polyamide seeding particles. In one of the tanks, 5 mL of the fluorescent dye (Rhodamine 6G) in a solution of 2 g/L, is also added giving a concentration of 40 μg/mL Rh6G. The flow is pumped from the storage tanks via one flow-meter for each tank to control the flow-rate in the mixing channel.

The three measurement positions are shown in Figure 1. The mixing is investigated in the initial mixing zone (Positions 1 and 2) and towards the end of the mixing channel (Position 3). The measurements are made in the $xy$-plane,

yielding the $U$ and $V$ velocity components in the $x$ and $y$ directions, respectively. Measurements are performed for three different flow cases, given in Table 1. For case 1, the bulk velocities in the feed channels are 0.17 m/s, which give a Reynolds number based on feed channel hydraulic diameter of 5100. The bulk velocity in the main channel is 0.11 m/s, which gives a Reynolds number based on main channel hydraulic diameter of 6600. The bulk concentration in feed channel A, $C_{A,b}$ is normalized to $\xi_A = C_A/C_{A,b} = 1$ and the bulk concentration in feed channel B, is $\xi_B = C_B/C_{B,b} = 0$ for all three flow cases.

**Table 1.** Inlet bulk velocities for the different flow cases.

| | Velocity (m/s) | | Velocity ratio |
|---|---|---|---|
| Case | Inlet A ( $V_{A,b}$ ) | Inlet B ( $V_{B,b}$ ) | ( $V_{A,b} : V_{B,b}$ ) |
| 1 | 0.17 | 0.17 | 1.:1 |
| 2 | 0.085 | 0.17 | 0.5:1 |
| 3 | 0.0425 | 0.17 | 0.25:1 |

## 2.2 Data analysis

The response of the fluorescent light is monitored with 6 different dye concentrations in the system. This is done to ensure linear response to the dye concentration. In Figure 2, a typical point calibration curve for the mean fluorescence signal including the statistical 95% limits (+/- 2 standard deviations) is shown. More details about the calibration of the measurement system are given in Hjertager Osenbroch (2004).

Before recording the actual measurements the background emission is recorded by taking a series of 20 background images at each measurement position with no dye present in the water, i.e. a concentration, $C_0 = 0$ mg/L. An average of 20 images corresponds to the intensity of the mean background noise, $I_{back}$ and this is used to set the zero value for the cameras response on variation in dye concentration. The optical system imperfections are mapped in a reference image where the concentration is homogeneous. The average of 20 images with maximum concentration, $C_{max} = 0.04$ mg/L, is used as reference, $I_{ref}$, at each measurement position. This is done to be able to compensate for variable light distribution in the laser-sheet. The processing of the data is performed as described by Hjertager Osenbroch (2004). To find the grey-levels representing maximum and minimum concentration, positions in the images with known concentrations are used as reference values. In the initial mixing zone, such areas are easy to find since the streams are not yet mixed. At the far end of the channel

it is more difficult, and an image from the initial zone has to be used as reference for this position as well. The images are scaled based on the maximum and minimum concentrations.
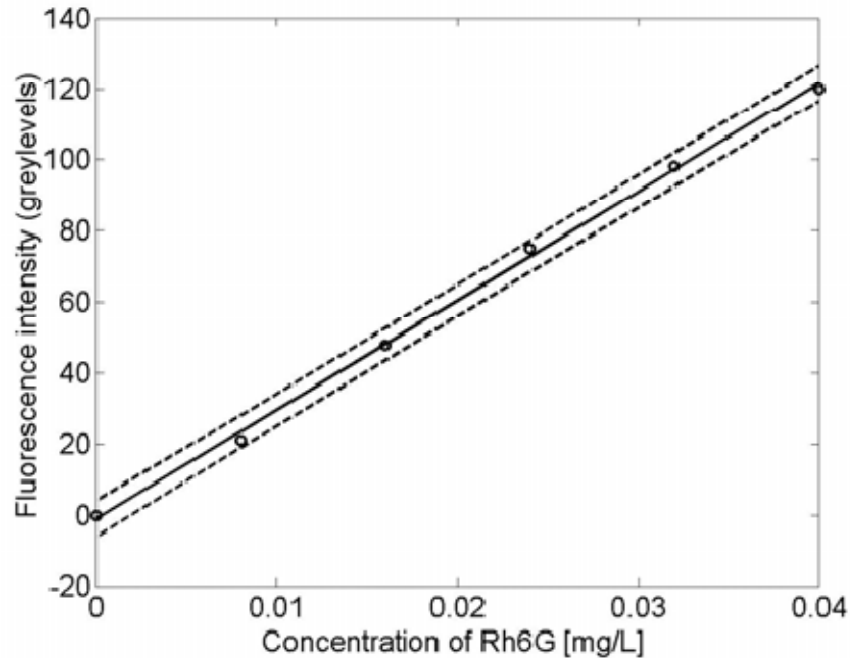


**Figure 2.** Fluorescence intensity versus concentration of Rh6G.

For the PIV recordings an exposure time delay between the two images of $\Delta t$ = 5 ms is used, the measurement area is approximately $67 \times 67$ mm$^2$ at the three different measurement locations. An adaptive correlation algorithm is used to capture both small and large velocities in the flow. The initial interrogation area for Position 1 is $64 \times 128$ px$^2$, and the final interrogation area is $32 \times 64$ px$^2$, which corresponds to an area of $2.1 \times 4.2$ mm$^2$. An overlap between interrogation areas of 50% horizontally and 75% vertically is used. For Positions 2 and 3, the initial interrogation area is $64 \times 64$ px$^2$, and the final interrogation area is $32 \times 32$ px$^2$, which corresponds to an area of $2.1 \times 2.1$ mm$^2$. An overlap between the interrogation areas of 50% is chosen for these cases. The size of the interrogation area is optimised for the velocities.

When the experiments are performed no cross-correlation between the two cameras is possible because of the equipment available. Instead the two cameras are carefully adjusted to have the same view. An error is introduced due to the fact

that the PIV and PLIF camera image do not overlap 100%. There is a displacement of up to 5 px, which corresponds to 0.35 mm. The PLIF-coordinates is set equal to the PIV-coordinates. This gives less precise results than what would have been obtained if the cameras are cross-correlated and the exact displacement between the two images could be used to find the exact PLIF-coordinates according to the PIV-coordinates.

For the determination of ensemble-averaged velocity and concentration fields and turbulence statistics, 200 image pairs are used. At $y/d = 1$ for the axial velocity $(V)$ and the concentration $(C)$, with a 95% confidence interval, the error is about 3.5 % for the mean and about 10% for the standard deviation.

## 3. GOVERNING EQUATIONS

### 3.1 Modelling of flow and turbulence

Turbulent flows of incompressible Newtonian fluids are governed by the Reynolds Averaged Navier-Stokes (RANS) equations. Assuming the flow to be steady and two-dimensional, the continuity and the momentum equations for the mean flow may be written in Cartesian tensor notation as

$$\frac{\partial U_j}{\partial x_j} = 0 \tag{1}$$

$$\frac{\partial}{\partial x_j}\left(\rho U_j U_i\right) = -\frac{\partial P}{\partial x_i} + \frac{\partial \tau_{ij}}{\partial x_j} \tag{2}$$

Here, $\rho$ is the density, $U_i$ is the mean velocity in the $x_i$-direction, $P$ is the pressure and $\tau_{ij} = -\rho \overline{u'_i u'_j}$ are the turbulent Reynolds stresses.

The transport of a passive scalar $\phi$ in a turbulent flow is governed by a convection-diffusion equation of the form

$$\frac{\partial}{\partial x_j}\left(\rho U_j \phi\right) = -\frac{\partial J_{\phi,j}}{\partial x_j} \tag{3}$$

where $J_{\phi,j} = -\rho \overline{u'_j \phi'}$ are the turbulent Reynolds scalar fluxes.

The effects of the turbulence on the mean flow are modelled by an eddy viscosity model. Accordingly, the turbulent Reynolds stresses are modelled in analogy with laminar stresses as

$$\tau_{ij} = -\rho \overline{u_i' u_j'} = 2\mu_T S_{ij} - \frac{2}{3}\delta_{ij}\rho k \tag{4}$$

where the mean rate-of-strain is given by

$$S_{ij} = \frac{1}{2}\left( \frac{\partial U_i}{\partial x_j} + \frac{\partial U_j}{\partial x_i} \right) \tag{5}$$

Likewise, the turbulent Reynolds scalar fluxes are modelled using the gradient-diffusion hypothesis as

$$J_{\phi,j} = \rho \overline{u_j' \phi'} = -\Gamma_\phi \frac{\partial \phi}{\partial x_j} \tag{6}$$

Using a $k - \varepsilon$ turbulence model, the turbulent viscosity $\mu_T$ can be defined by the turbulent kinetic energy $k$ and its dissipation rate $\varepsilon$ as

$$\mu_T = C_\mu \rho \frac{k^2}{\varepsilon} \tag{7}$$

The turbulent transport coefficient or diffusivity $\Gamma_\phi$ is related to the turbulent viscosity by the turbulent Prandtl/Schmidt number $\sigma_\phi$ as

$$\Gamma_\phi = \frac{\mu_T}{\sigma_\phi} \tag{8}$$

Three $k - \varepsilon$ turbulence models have been considered, namely the standard $k - \varepsilon$ model (Versteeg and Malalaskera, 1996), the RNG $k - \varepsilon$ model (Versteeg and Malalaskera, 1996) and the Chen-Kim $k - \varepsilon$ model (Schmalzriedt et al., 2003). The transport equations for the turbulent kinetic energy and its dissipation rate can be summarized as

$$\frac{\partial}{\partial x_j}\left(\rho U_j k\right) = \frac{\partial}{\partial x_j}\left(\Gamma_k \frac{\partial k}{\partial x_j}\right) + P_k - \rho \varepsilon \tag{9}$$

$$\frac{\partial}{\partial x_j}\left(\rho U_j \varepsilon\right) = \frac{\partial}{\partial x_j}\left(\Gamma_\varepsilon \frac{\partial \varepsilon}{\partial x_j}\right) + \frac{\varepsilon}{k}\left(C_1(\eta) P_k - C_2 \rho \varepsilon\right) \tag{10}$$

Here, the production of turbulent kinetic energy $P_k$ is expressed in terms of the mean strain rate $S = \sqrt{2S_{ij}S_{ij}}$ as

$$P_k = \tau_{ij}\frac{\partial U_i}{\partial x_j} = \mu_T S^2 \tag{11}$$

In the dissipation rate transport equation, the modelling parameter $C_1$ is noted to be made sensitive to the timescale ratio between the turbulence and the mean flow, i.e. $\eta = S k/\varepsilon$. The modelling parameters for the various versions of the $k - \varepsilon$ turbulence models are given in Table 2.

**Table 2.** Modelling parameters for the various $k - \varepsilon$ turbulence models.

| Models | $C_\mu$ | $C_1(\eta)$ | $C_2$ | $C_3$ | $\sigma_k$ | $\sigma_\varepsilon$ | $\beta$ | $\eta_0$ |
|---|---|---|---|---|---|---|---|---|
| Standard | 0.0900 | 1.44 | 1.92 | - | 1.0 | 1.3 | - | - |
| RNG | 0.0845 | $1.42 + \dfrac{\eta\left(\dfrac{\eta}{\eta_0}-1\right)}{(1+\beta\eta)}$ | 1.68 | - | 0.72 | 0.72 | 0.012 | 4.377 |
| Chen-Kim | 0.0900 | $1.15 + C_3 C_\mu \eta^2$ | 1.90 | 0.25 | 0.75 | 1.15 | - | - |

## 3.2 Mass transfer modelling

The multi-peak presumed PDF model by Fox (1998) represents the concentration PDF by a finite set of delta functions. In this approach, each control volume in the computational domain is divided into a finite number of homogeneous environments. Each environment corresponds to a discretization of the composition PDF in a finite set of delta functions as

$$f_\phi\left(\mathbf{\psi};\mathbf{x},t\right)=\sum_{n=1}^{N_e} p_n\left(\mathbf{x},t\right)\prod_{\alpha=1}^{N_s}\delta\left(\psi_\alpha-\left\langle\phi_\alpha\right\rangle_n\left(\mathbf{x},t\right)\right) \tag{12}$$

where $p_n$ is the probability of environment $n$, $\psi_\alpha$ is the concentration space coordinate of the scalar $\alpha$, $\left\langle\phi_\alpha\right\rangle_n$ is the mean concentration of the scalar $\alpha$ in environment $n$, $N_e$ is the total number of environments, and $N_s$ is the total number of scalars (Marchisio et al., 2001). The exchange of material between the environments allows the inlet streams to contact each other.
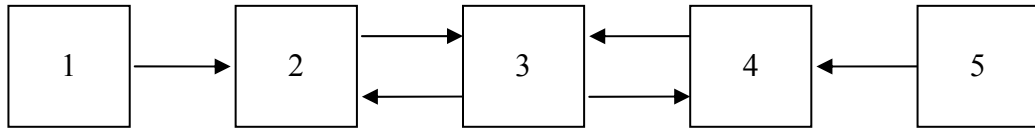


**Inlet stream 1**:

$<\xi>_1=1\ p_1=1$    $<\xi>_2<1$    $1>\ <\xi>_3>0$    $<\xi>_4>0$

**Inlet stream 2:**

$<\xi>_5=0\ p_5=1$

**Figure 3.** Illustration of the multi-peak model with 5 environments.

For steady mixing of two inlets streams without chemical reactions, the composition vector can be described by a single mixture fraction, i.e. $\phi=\xi$. Figure 3 shows an illustration of the present multi-peak model where the total number of environments is taken as five, i.e. $N_e=5$. Each environment $n$ is described by the local mixture fraction $\left\langle\xi\right\rangle_n$, the local volume fraction $p_n$ and the local volume-weighted mixture fraction $\left\langle s_\xi\right\rangle_n=p_n\left\langle\xi\right\rangle_n$.

The Reynolds averaged transport equation for the volume fraction may be written as

$$\frac{\partial}{\partial x_j}\left(\rho U_j p_n\right)=\frac{\partial}{\partial x_j}\left(\Gamma_T\frac{\partial p_n}{\partial x_j}\right)+\rho G_n\left(p\right)+\rho G_{sn}\left(p\right) \tag{13}$$

The probability exchange rates $G_n\left(p\right)$ that give the change in $p_n$ due to micromixing are taken as

$$
\begin{aligned}
G_1(p) &= -r_1(p) \\
G_2(p) &= r_1(p) - r_2(p) + r_3(p) \\
G_3(p) &= r_2(p) - 2r_3(p) + r_4(p) \\
G_4(p) &= r_3(p) - r_4(p) + r_5(p) \\
G_5(p) &= -r_5(p)
\end{aligned}
\tag{14}
$$

The probability fluxes $r_n(p)$ defined in terms of the micromixing rate $\gamma$ are taken as

$$
\begin{aligned}
r_1(p) &= \gamma p_1(1 - p_1) \\
r_2(p) &= \gamma p_2 \\
r_3(p) &= \gamma p_3 \\
r_4(p) &= \gamma p_4 \\
r_5(p) &= \gamma p_5(1 - p_5)
\end{aligned}
\tag{15}
$$

Global conservation of mass requires that $\sum_{n=1}^{N_e} G_n(p) = 0$ and $\sum_{n=1}^{N_e} p_n = 1$.

The Reynolds averaged transport equation for the volume-weighted mixture fraction may be written as

$$
\frac{\partial}{\partial x_j}\left(\rho U_j \langle s_\xi \rangle_n\right) = \frac{\partial}{\partial x_j}\left(\Gamma_T \frac{\partial \langle s_\xi \rangle_n}{\partial x_j}\right) + \rho M_\xi^n(p,s) + \rho M_{s\xi}^n(p,s)
\tag{16}
$$

The scalar fluxes between environments $M_\xi^n(p,s)$, which account for micromixing are taken as

$$M_\xi^1(p,s) = -r_1(p)\langle\xi\rangle_1$$
$$M_\xi^2(p,s) = r_1(p)\langle\xi\rangle_1 - r_2(p)\langle\xi\rangle_2 + r_3(p)\langle\xi\rangle_3$$
$$M_\xi^3(p,s) = r_2(p)\langle\xi\rangle_2 - 2r_3(p)\langle\xi\rangle_3 + r_4(p)\langle\xi\rangle_4 \tag{17}$$
$$M_\xi^4(p,s) = r_3(p)\langle\xi\rangle_3 - r_4(p)\langle\xi\rangle_4 + r_5(p)\langle\xi\rangle_5$$
$$M_\xi^5(p,s) = -r_5(p)\langle\xi\rangle_5$$

Conservation of mass requires again that $\sum_{n=1}^{N_e} M_\xi^n(p,s) = 0$.

The local mixture fraction $\langle\xi\rangle_n$ in environment $n$, the mean mixture fraction $\langle\xi\rangle$ and the mixture-fraction variance $\langle\xi'^2\rangle$ can be expressed by

$$\langle\xi\rangle_n = \frac{\langle s_\xi\rangle_n}{p_n} \tag{18}$$

$$\langle\xi\rangle = \sum_{n=1}^{N_e}\langle s_\xi\rangle_n \tag{19}$$

and

$$\langle\xi'^2\rangle = \sum_{n=1}^{N_e}\frac{\langle s_\xi\rangle_n^2}{p_n} - \langle\xi\rangle^2 \tag{20}$$

A transport equation for the mixture-fraction variance which is often used in mixing models can be derived from its definition in Eq. (20) using the transport equations for the volume fraction and the volume-weighted mixture fraction given in Eqs. (13) and (16). In the multi-peak presumed PDF model, a *spurious* dissipation term appears in the mixture-fraction-variance transport equation for inhomogeneous flows. This *spurious* dissipation term is unphysical and is due to the presumed form of the composition PDF with a finite set of delta functions. The *spurious* dissipation term can be removed by introducing two additional micromixing terms $G_{sn}$ and $M_{s\xi}^n$. These additional micromixing terms are, however, discarded in the present work as they will be model dependent and because they are expected to become smaller with increasing number of delta functions or environments (Piton et al., 2000). The *spurious* dissipation term can

be handled in a general manner by the direct quadrature method of moments (DQMOM) as described by Wang and Fox (2004).

The rate of micromixing $\gamma$ can be defined as $\gamma = 1/\tau_m$ where $\tau_m$ is the characteristic timescale for micromixing. The micromixing timescale tested is a simple large-scale-eddy motion model. The characteristic micromixing timescale is expressed by $\tau_m = \left(1/C_\phi\right)\left(k/\varepsilon\right)$, where $C_\phi = 1$ for fully-developed turbulence. For moderate Reynolds numbers close to the transition region and when taking account of the fact that the scalar field near the injection point is not fully developed a value of $C_\phi = 0.5$ have been used by others (Fox, 1998 and Piton et al., 2000). In this work, we use $C_\phi = 1$.

**Table 3.** Inlet boundary conditions for the mixing case with 5 environments.

| | Inlet stream | |
|---|---|---|
| Variable | A | B |
| $p_1$ | 1 | 0 |
| $p_2$ | 0 | 0 |
| $p_3$ | 0 | 0 |
| $p_4$ | 0 | 0 |
| $p_5$ | 0 | 1 |
| $\langle s_\xi \rangle_1$ | 1 | 0 |
| $\langle s_\xi \rangle_2$ | 0 | 0 |
| $\langle s_\xi \rangle_3$ | 0 | 0 |
| $\langle s_\xi \rangle_4$ | 0 | 0 |
| $\langle s_\xi \rangle_5$ | 0 | 0 |

For a pure mixing case without any reaction, transport equations for the volume fractions $p_n$ and the volume-weighted mixture fractions $\langle s_\xi \rangle_n$ have to be solved. The volume fractions have to be solved for in all 5 environments. Since the mixture fraction is constant in environment 1 and 5, the volume-weighted mixture fraction must only be solved for in environments 2, 3 and 4, i.e. $\langle s_\xi \rangle_2$, $\langle s_\xi \rangle_3$ and $\langle s_\xi \rangle_4$. This gives a total of 8 transport equations for the multi-peak presumed PDF model. Table 3 gives the inlet boundary conditions for the mixing case with 5 environments and two inlet streams.

## 4. RESULTS

### 4.1 Concentration experiments

Figure 4 shows the instantaneous concentration fields in the initial mixing zone (position 1 and 2), and towards the end of the channel (position 3) for the three flow cases. The experimental results for case 1 have previously been presented in Hjertager et al. (2003) but are repeated here for completeness. The concentration fields are noticed to be quite inhomogeneous following the large-scale transverse velocity fluctuations in the two images which represent the initial mixing zone, except for the recirculation region attached to the block dividing the mixing channel into two feed channels. In the image towards the end of the channel, the concentration fields are somewhat more homogeneous.

Figures 5 and 6 show the measured time averaged mean and fluctuating concentrations in the initial mixing zone for all three flow cases. For case 1 with an inlet velocity ratio of 1:1, the flow acts as a wake flow. Hence, the mixing layer is symmetric about the centreline and grows rapidly downstream. The concentration fluctuations are most dominant along the centreline. For case 2 with an inlet velocity ratio of 0.5:1, a weak backflow along the left channel wall is identified. This indicates that there is a transition from a wake flow towards a backward-facing step flow. The mixing layer is narrower and is shifted towards the channel with higher inlet velocity. The concentration fluctuations are lower indicating a lower mixing rate. For case 3 with an inlet velocity ratio of 0.25:1, the backflow along the left channel wall is much stronger. The flow seems now to act more like a backward-facing step flow. The mixing layer follows the separating shear layer that evolves from the block. The concentration fluctuations are again lower, indicating an even lower mixing rate. There is, however, a strong mixing in the recirculation region along the left channel wall.

As the velocity ratio is reduced and the flow behaviour changes from wake toward backward-facing step, the-large scale transverse velocity fluctuations are observed to be significantly reduced (see Figure 4).
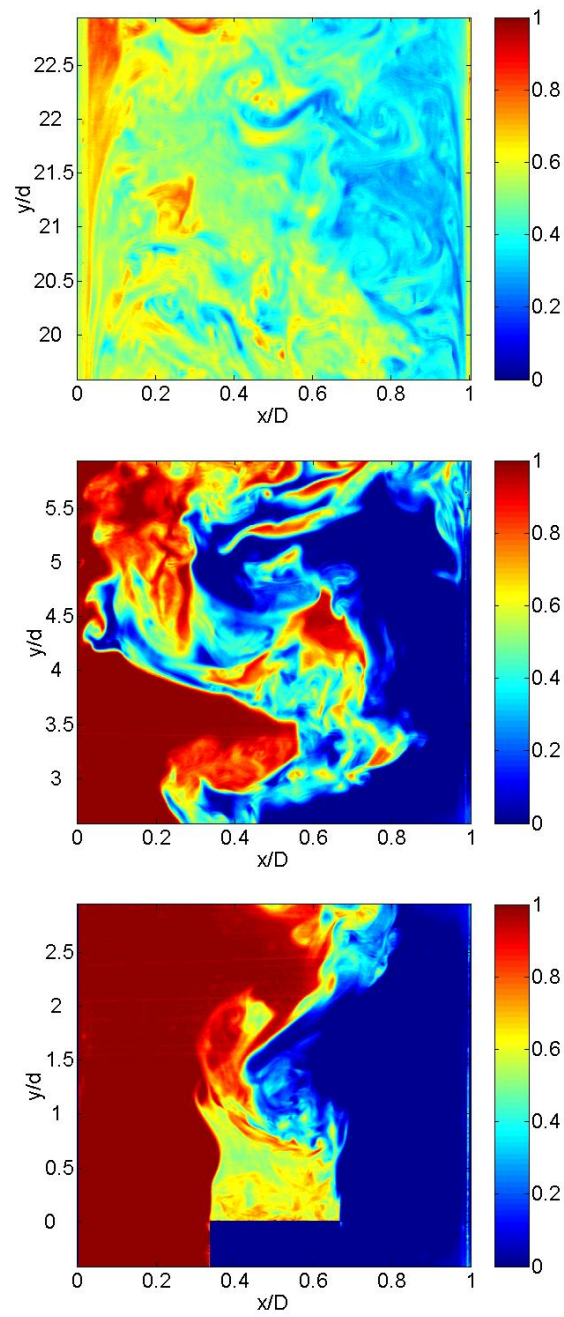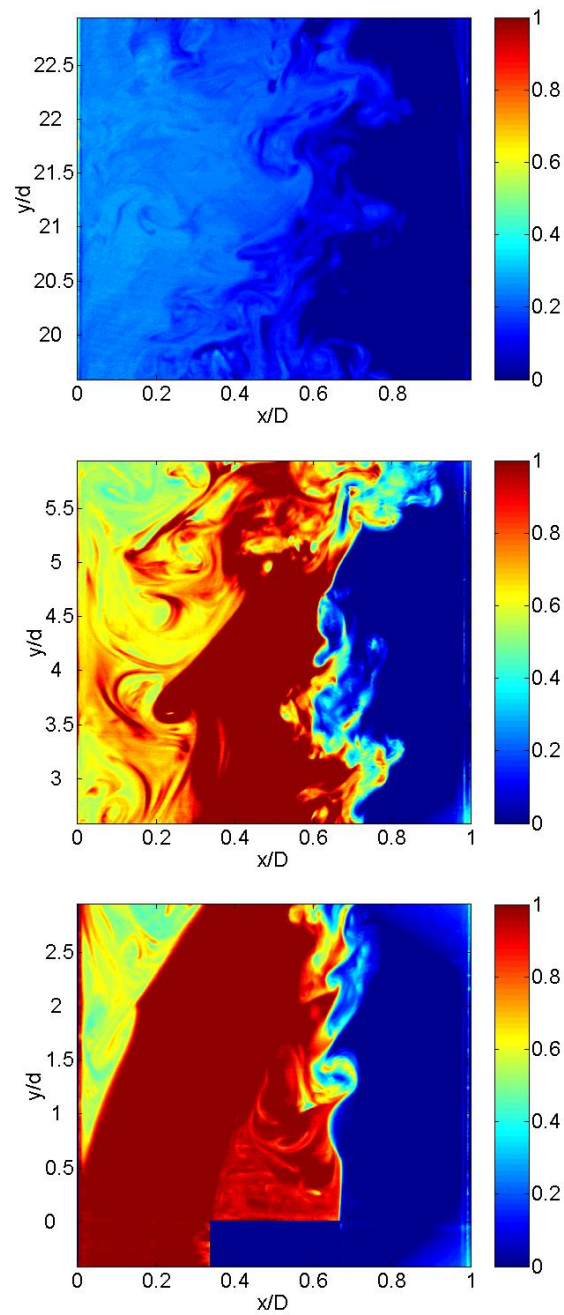
$$( V_{A,b} : V_{B,b} ) = (1\!:\!1)$$

**Figure 4.** Continued.
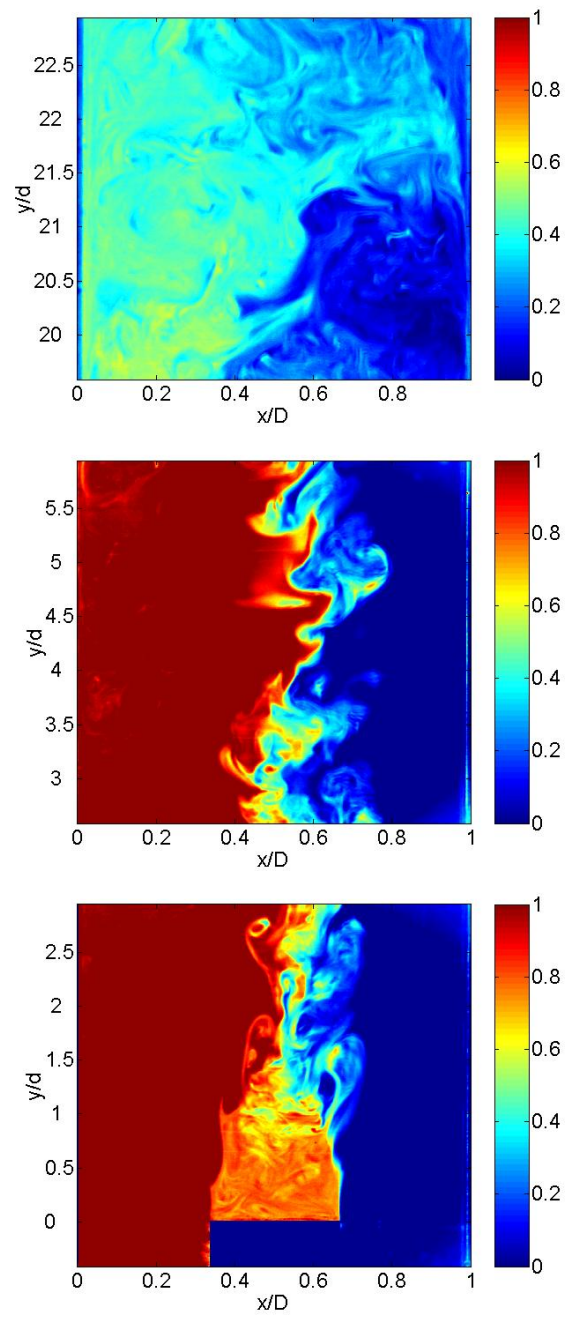
$$( V_{A,b} : V_{B,b} ) = (0.5{:}1)$$

**Figure 4.** Continued.

$$( \mathrm{V}_{A,b} : \mathrm{V}_{B,b} ) = (0.25{:}1)$$

**Figure 4.** Instantaneous concentration fields at different measurement positions along the channel for the three flow cases.
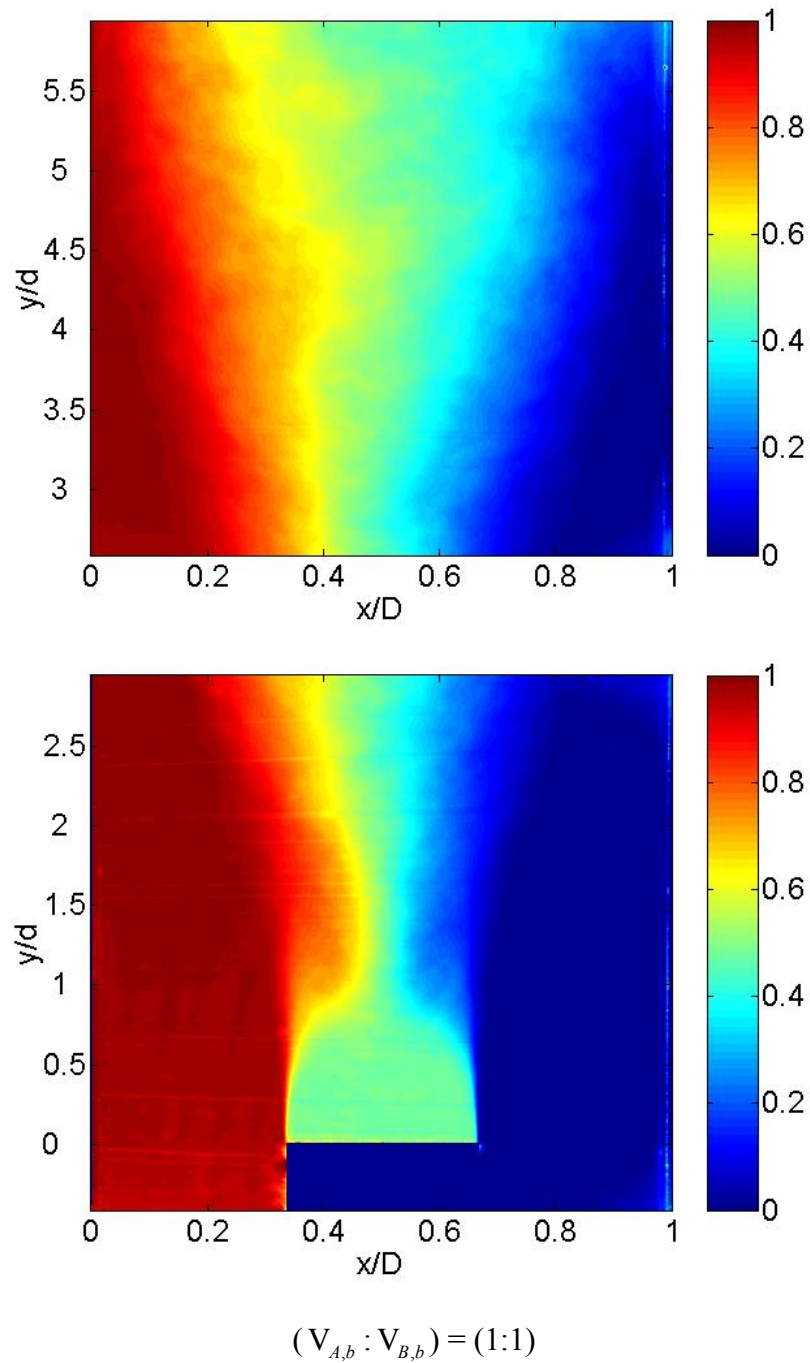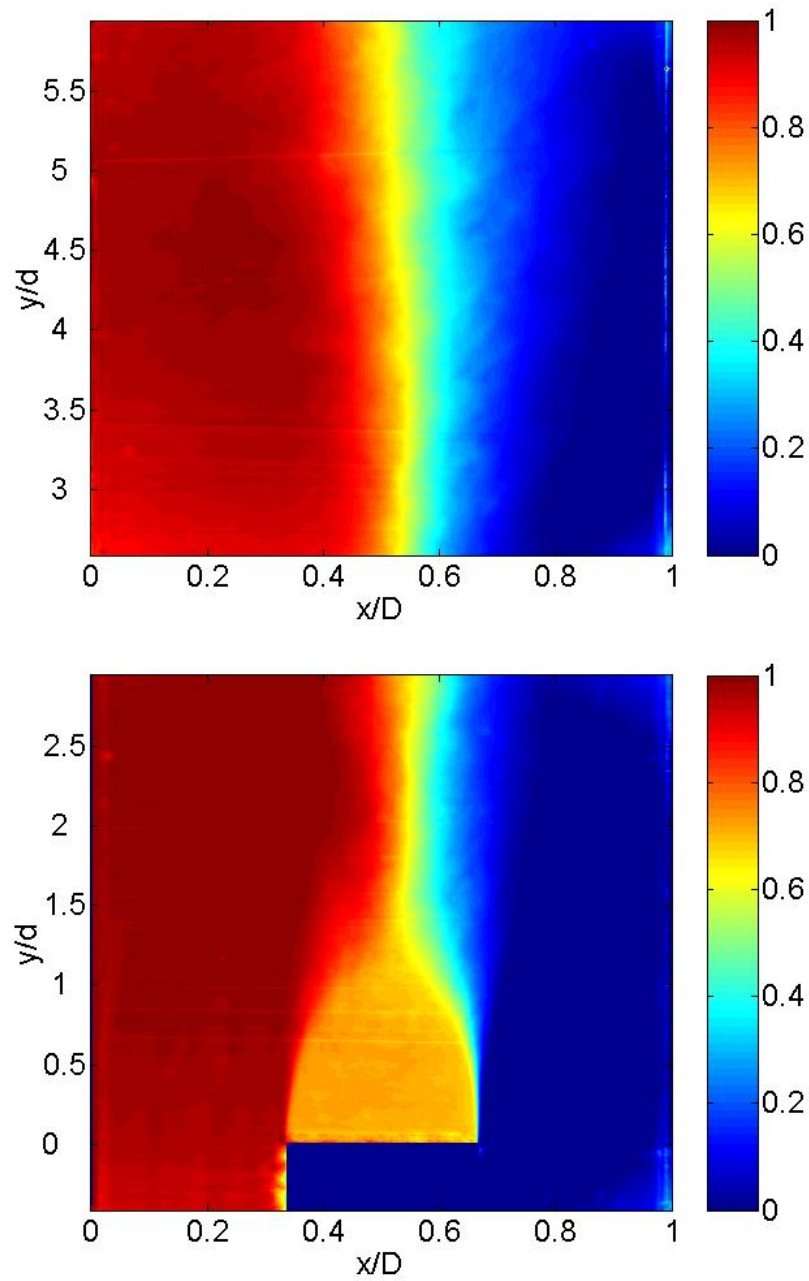
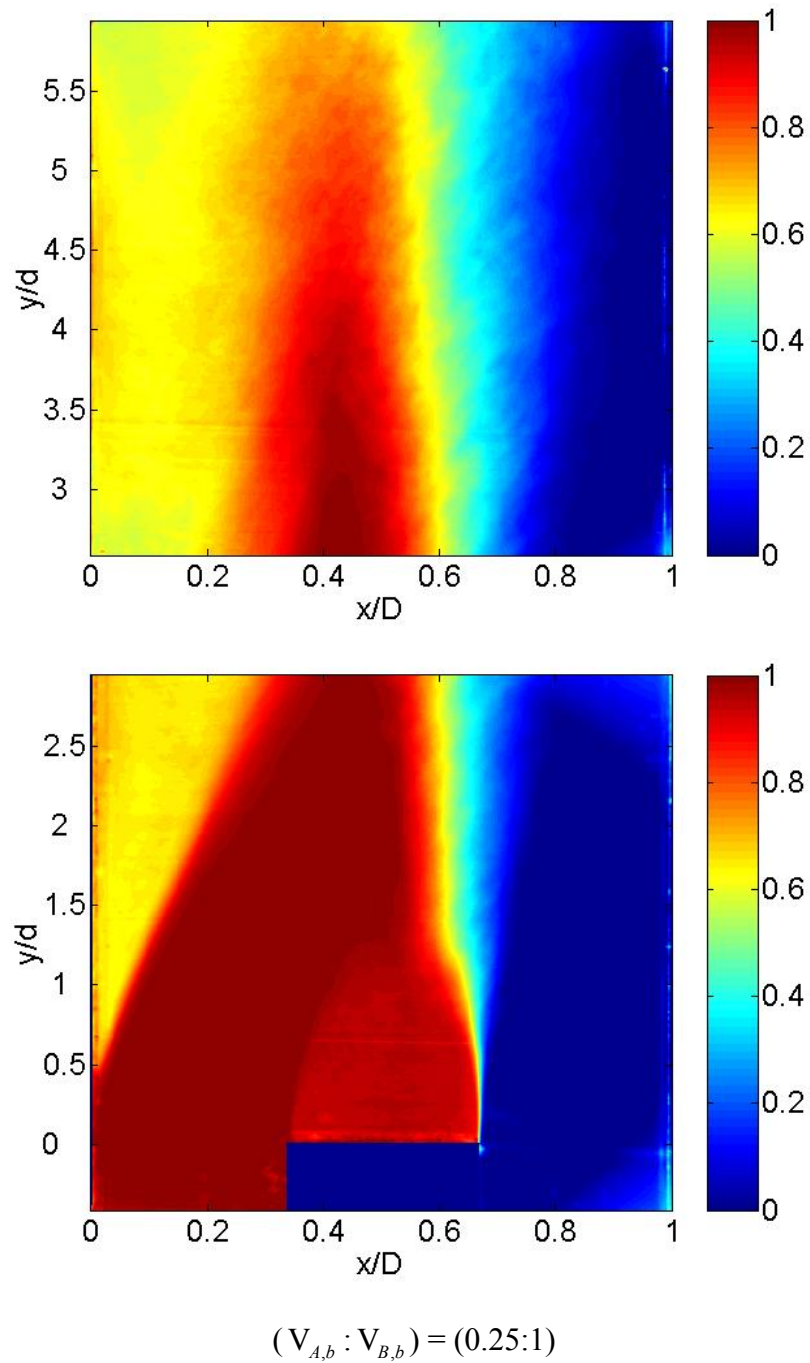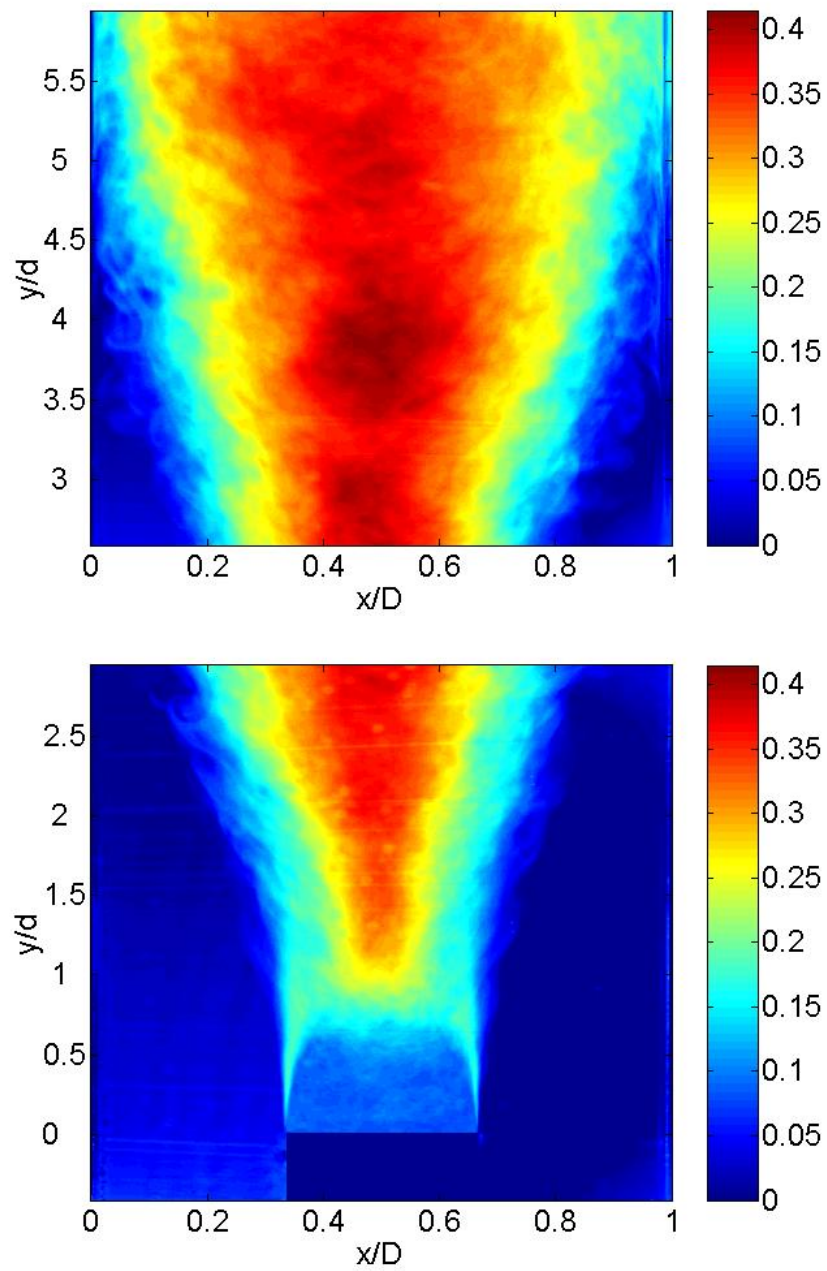$$( V_{A,b} : V_{B,b} ) = (1:1)$$

**Figure 5.** Continued.

$$( V_{A,b} : V_{B,b} ) = (0.5{:}1)$$

**Figure 5.** Continued.

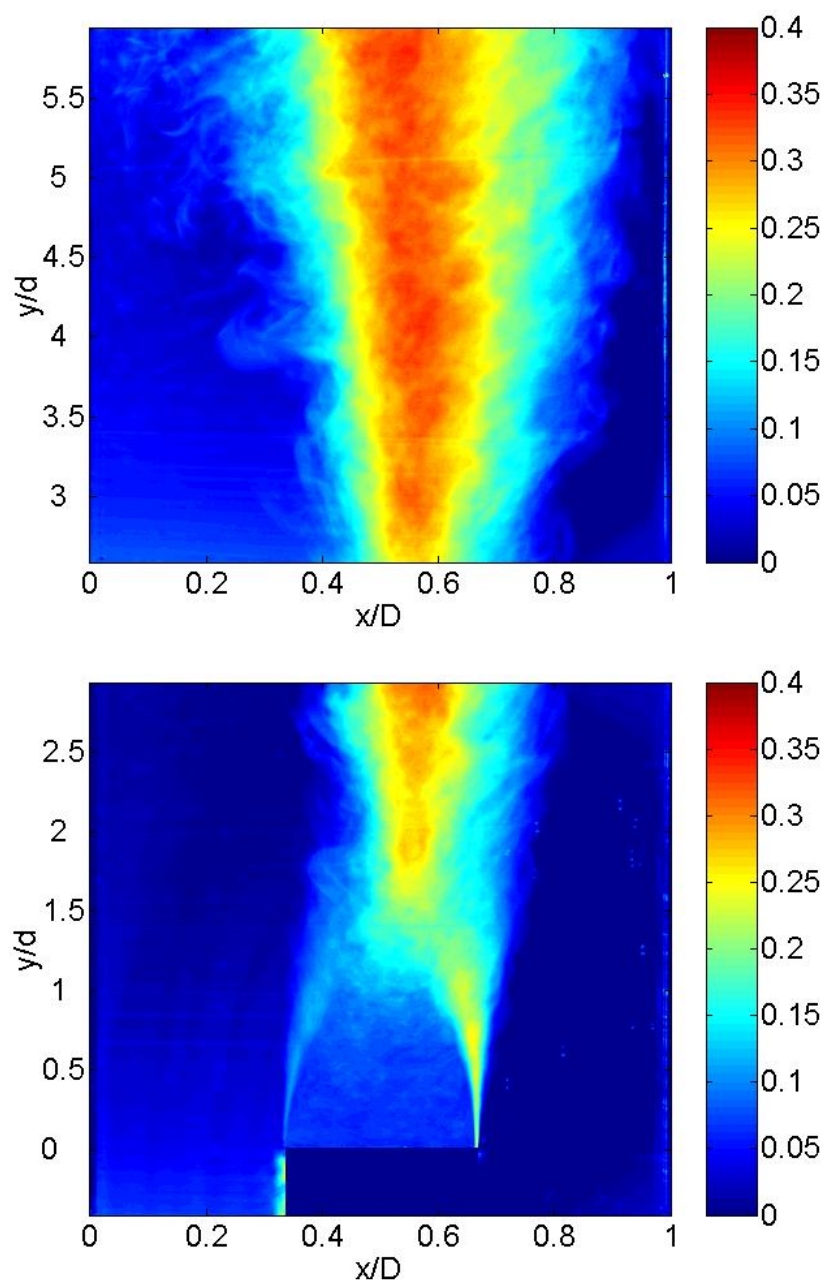$$(V_{A,b} : V_{B,b}) = (0.25{:}1)$$

**Figure 5.** Measured mean concentration in the initial mixing zone (positions 1 and 2) for the three flow cases.

$$( V_{A,b} : V_{B,b} ) = (1{:}1)$$

**Figure 6.** Continued.

$$( V_{A,b} : V_{B,b} ) = (0.5{:}1)$$

**Figure 6.** Continued.

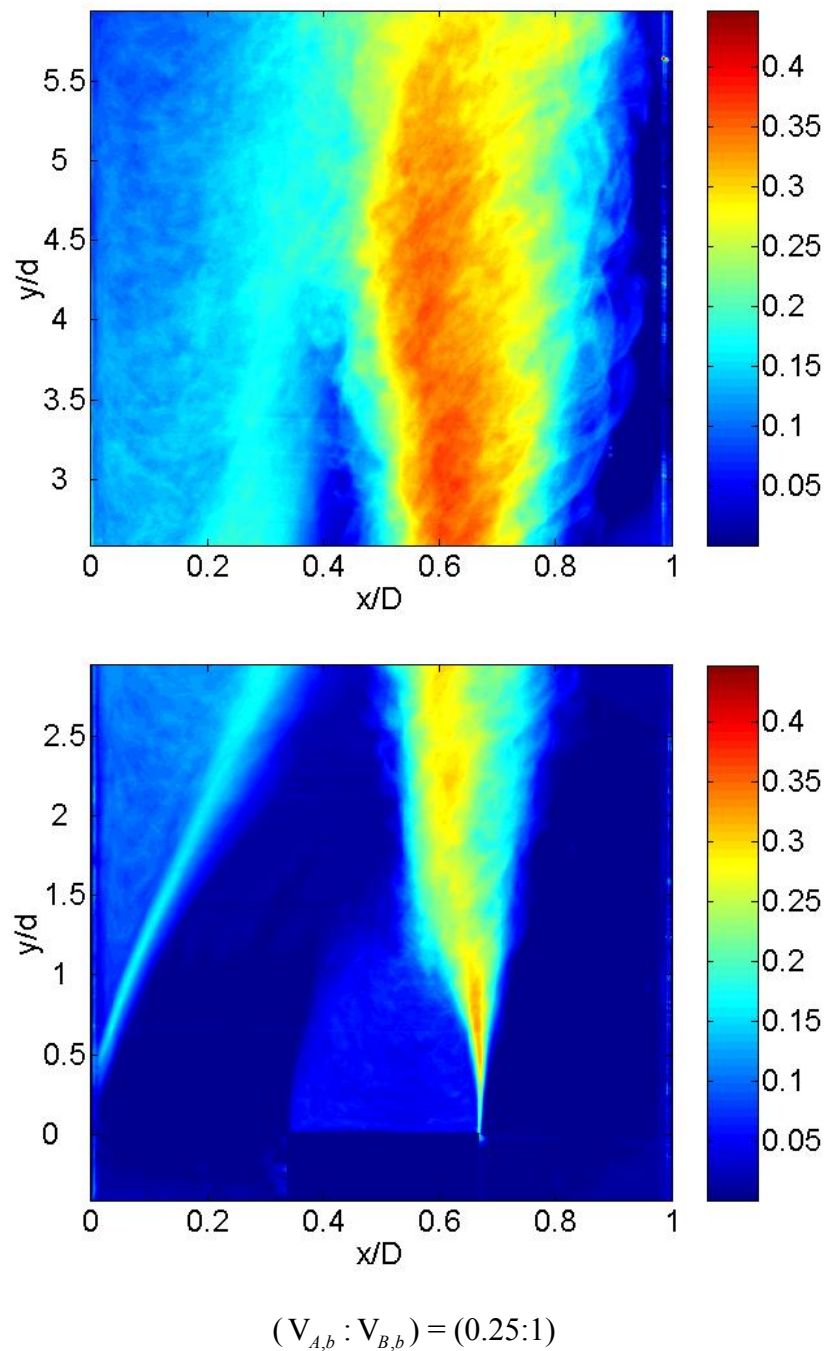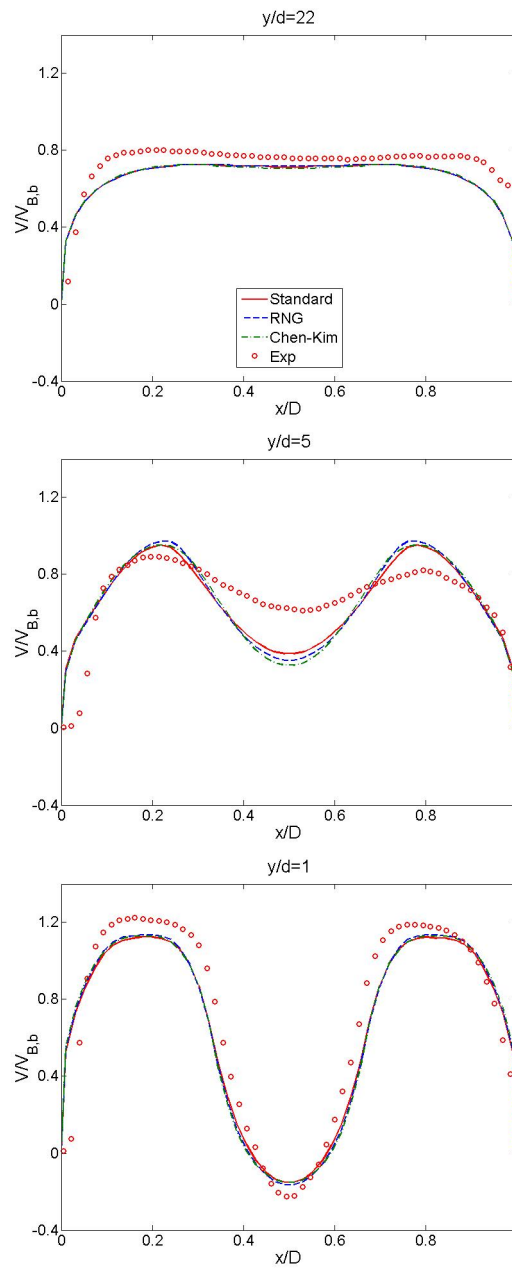$$( V_{A,b} : V_{B,b} ) = (0.25{:}1)$$

**Figure 6.** Measured concentration fluctuations in the initial mixing zone (positions 1 and 2) for the three flow cases.

## 4.2 Velocity measurements and predictions

The different $k - \varepsilon$ turbulence models show very little difference in predicting the velocity and concentration fields. A comparison of predicted and measured mean and fluctuating velocities for the three flow cases is shown in Figures 7 and 8. In general, the turbulence models are seen to be unable to capture the energy containing large scale fluctuating motion in the near wake observed in the measurements. The turbulence levels are seen to be predicted significantly too low in the wake shear layers. Accordingly, the turbulent viscosity is predicted to be too low, and the recovery of the mean velocity defect in the wake is predicted to be too slow. By reducing the flow rate of one of the feed channels, there is a transition from wake flow towards backward-facing step flow. Consequently, the wake is shifted towards the wall with the lower flow rate in the feed channel, and the large scale eddies are damped by the presence of the wall. Since the fluctuating motion is not as large as for case 1, the flow predictions of case 2 and 3 are somewhat better. The $k - \varepsilon$ models are noted to be unable to predict the backflow observed in the measurements for both case 2 and 3. In case 3, the backflow is noted to be quite pronounced. In order to resolve the large scale fluctuating motion in the near wake, a Large-Eddy-Simulation (LES) would most likely be a better choice for a turbulence model than the $k - \varepsilon$ model in all three flow cases.

## 4.3 Concentration predictions

A comparison of predicted and measured mean concentration for case 1 shows in Figure 9 that the concentration like the velocity exhibits a too slow recovery in the wake. However, the growth rate of the concentration wake can be improved by reducing the turbulent Schmidt number, $\sigma_T = Sc_T$, from the standard value of 0.7 to 0.15. The prediction of the mean concentration for case 2 is good using a turbulent Schmidt number of 0.7, however reducing it to 0.5 gives some improvement. The mean concentration predicted for case 3 along the left side of the channel does not fit well with experimental data at all probably due to significant backflow in the measurements which is not predicted. Reducing the turbulent Schmidt number does not have a significant effect on the results for this case. The micromixing model shows in Figure 10 a similar improvement in the prediction of the concentration fluctuations by reducing the Schmidt number as for the predictions of the mean concentration. The predictions with the micromixing rate using the simple large-scale dominated model show good agreement with measurements for all three flow cases.
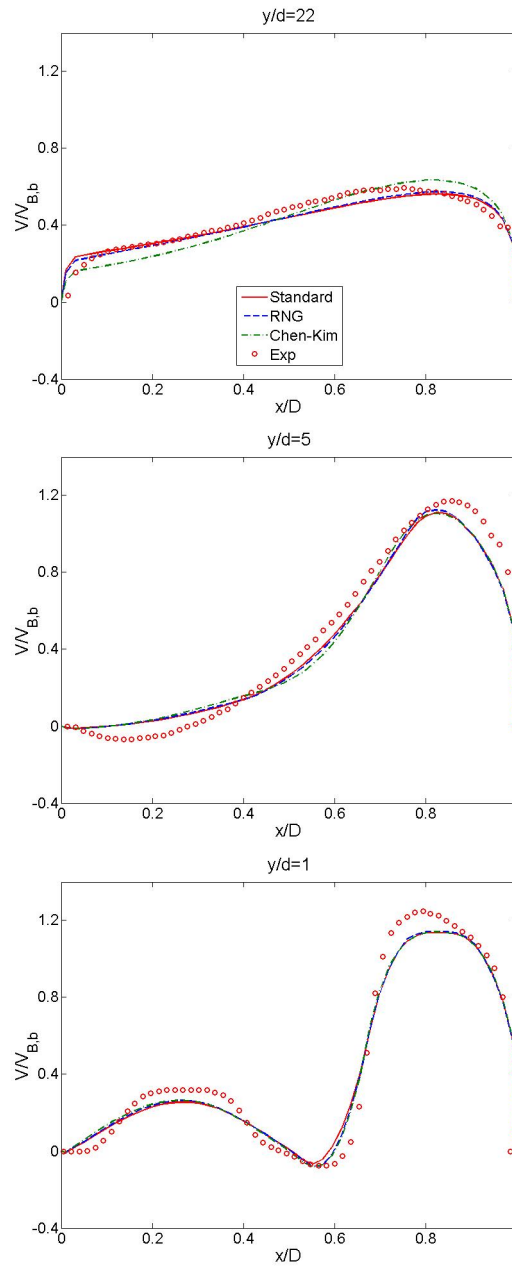
$$( \mathrm{V}_{A,b} : \mathrm{V}_{B,b} ) = (1{:}1)$$
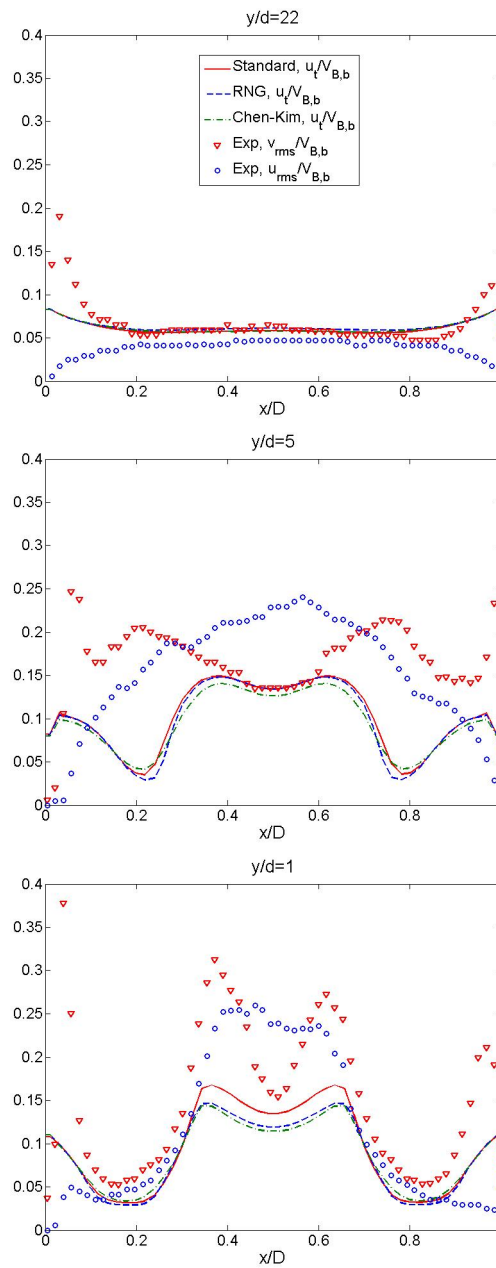
**Figure 7.** Continued.
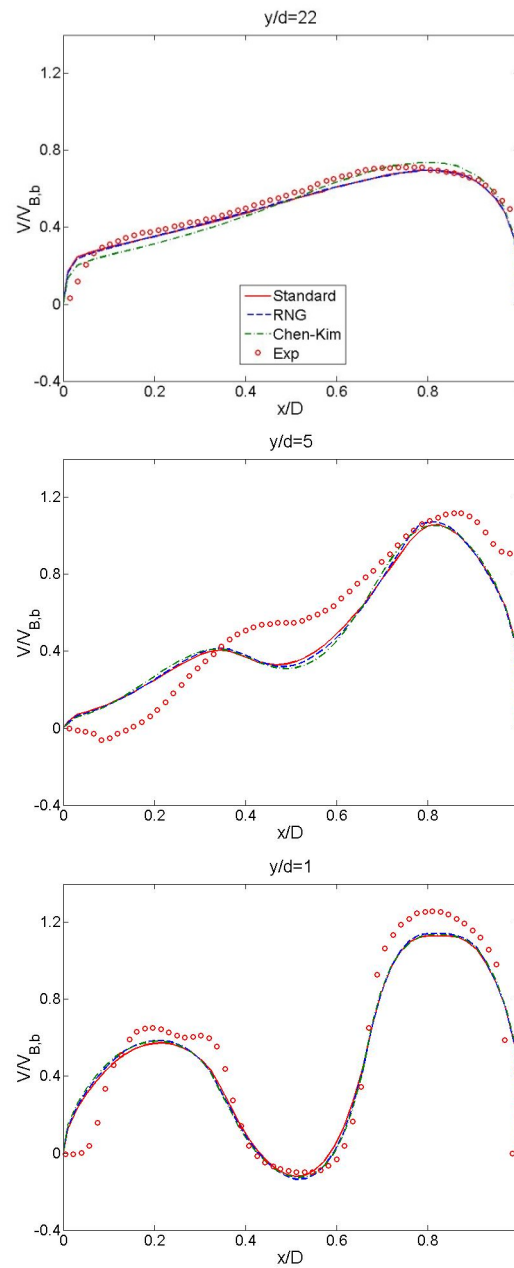
$$( V_{A,b} : V_{B,b} ) = (0.5{:}1)$$
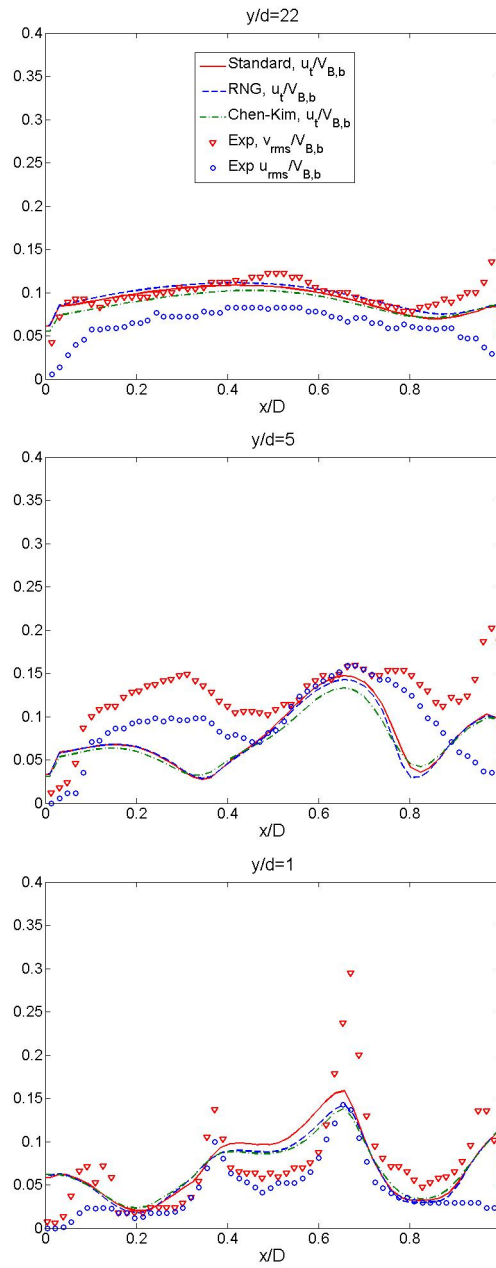
**Figure 7.** Continued.

$$( V_{A,b} : V_{B,b} ) = (0.25{:}1)$$

**Figure 7.** Measured and predicted axial mean velocity at different axial positions for the three flow cases.

$$( V_{A,b} : V_{B,b} ) = (1:1)$$

**Figure 8.** Continued.

$$( V_{A,b} : V_{B,b} ) = (0.5{:}1)$$

**Figure 8.** Continued.

$$(V_{A,b} : V_{B,b}) = (0.25 : 1)$$
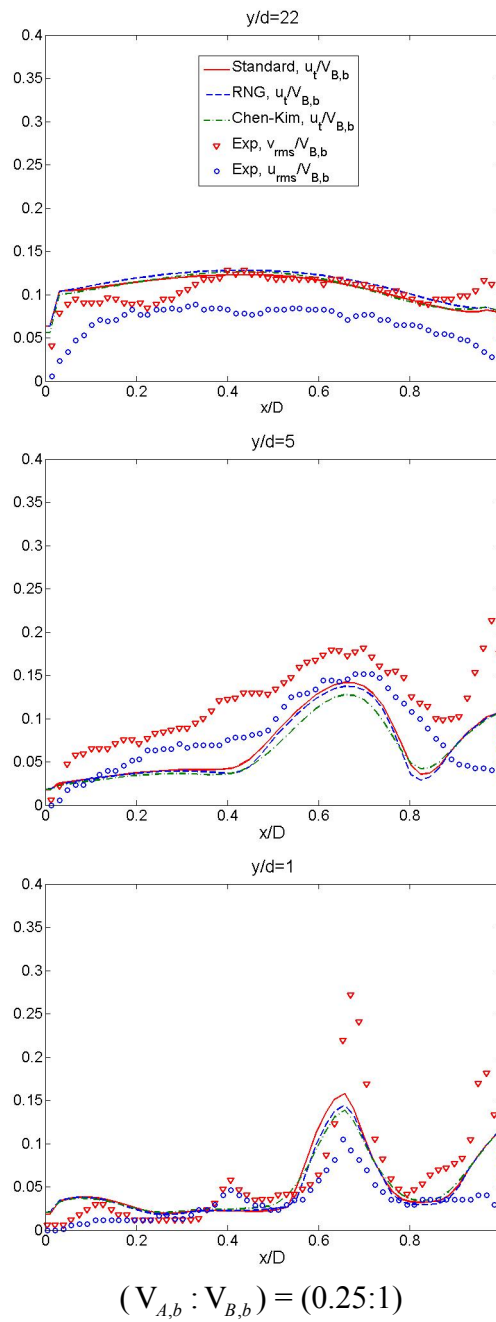
**Figure 8.** Measured and predicted axial turbulence velocity for the three flow cases.

$$( V_{A,b} : V_{B,b}) = (1{:}1)$$

**Figure 9.** Continued.

$$( V_{A,b} : V_{B,b} ) = (0.5{:}1)$$

**Figure 9.** Continued.

$(V_{A,b} : V_{B,b}) = (0.25:1)$

**Figure 9.** Measured and predicted mean concentration for the three flow cases.

$$( V_{A,b} : V_{B,b} ) = (1{:}1)$$

**Figure 10.** Continued.

$$( V_{A,b} : V_{B,b} ) = (0.5:1)$$
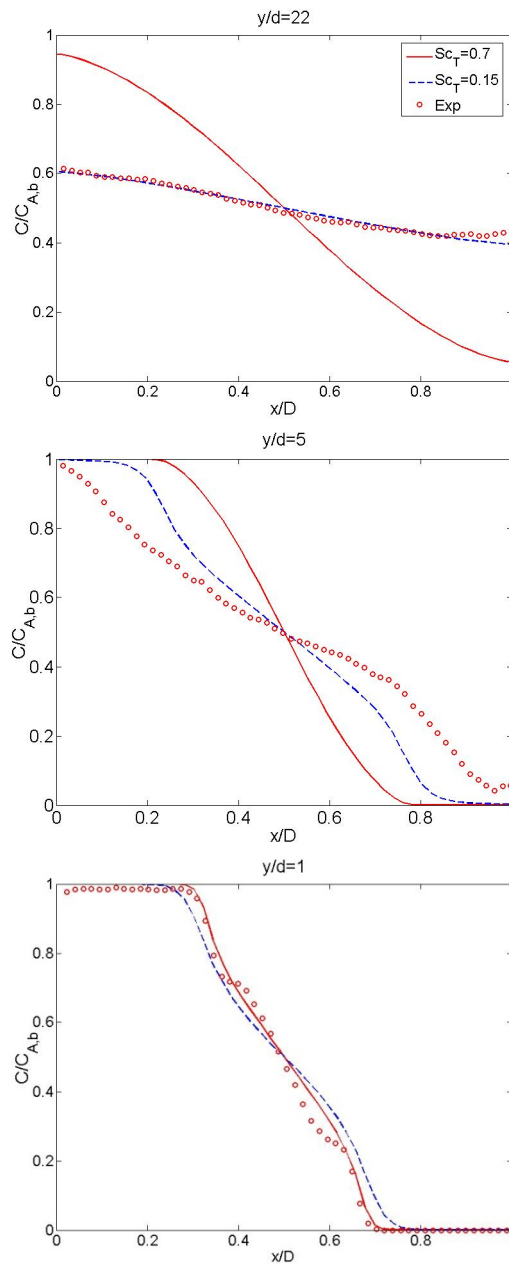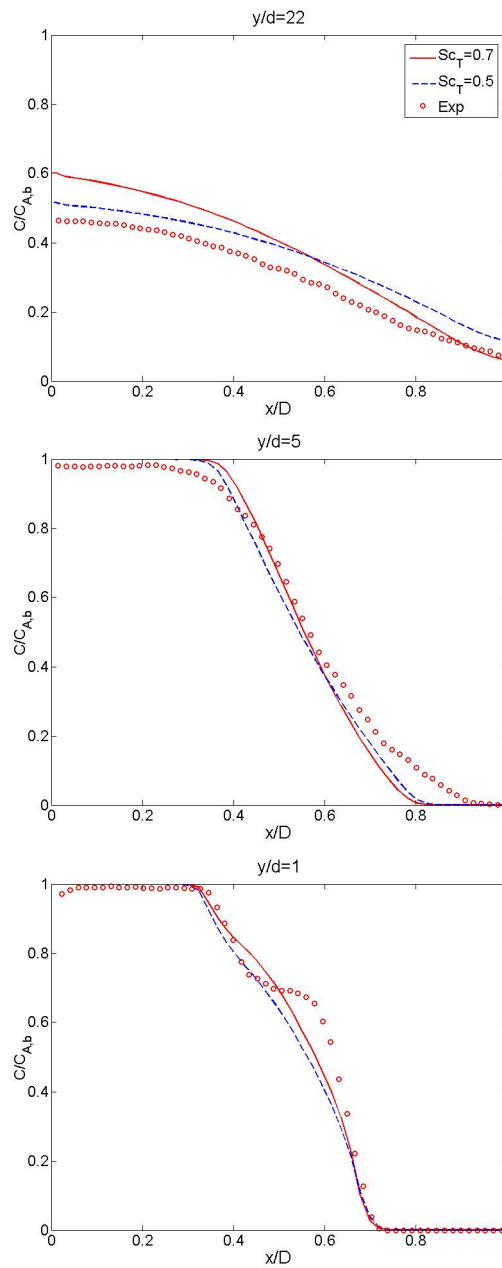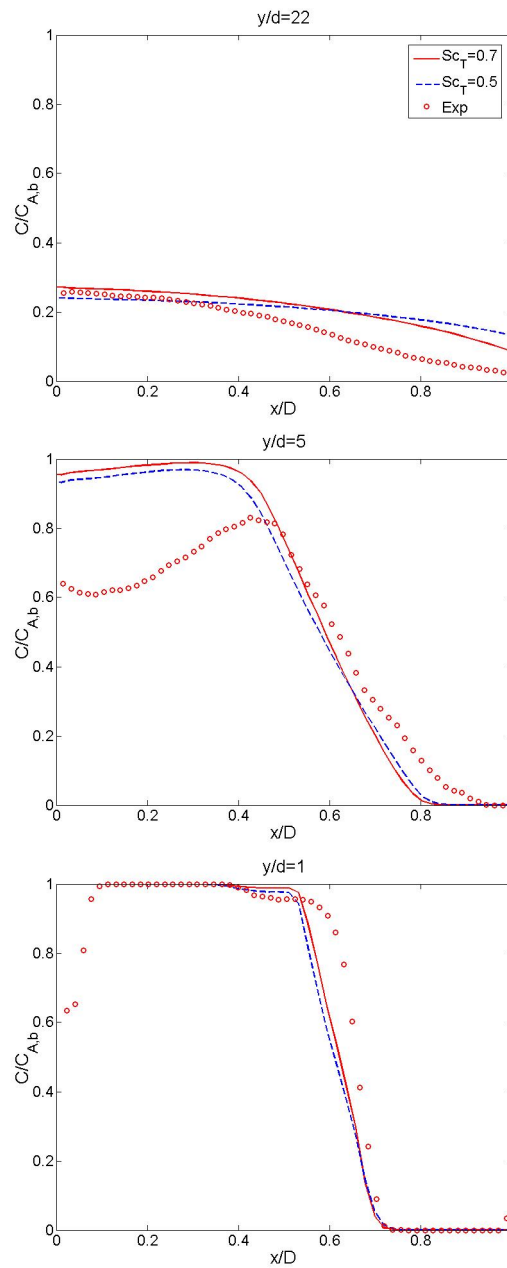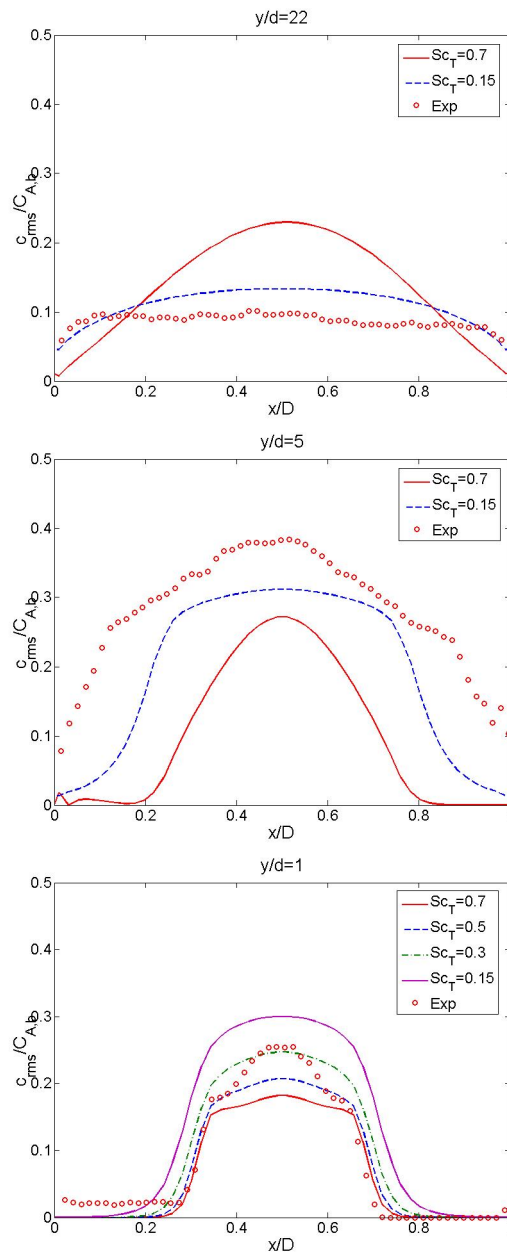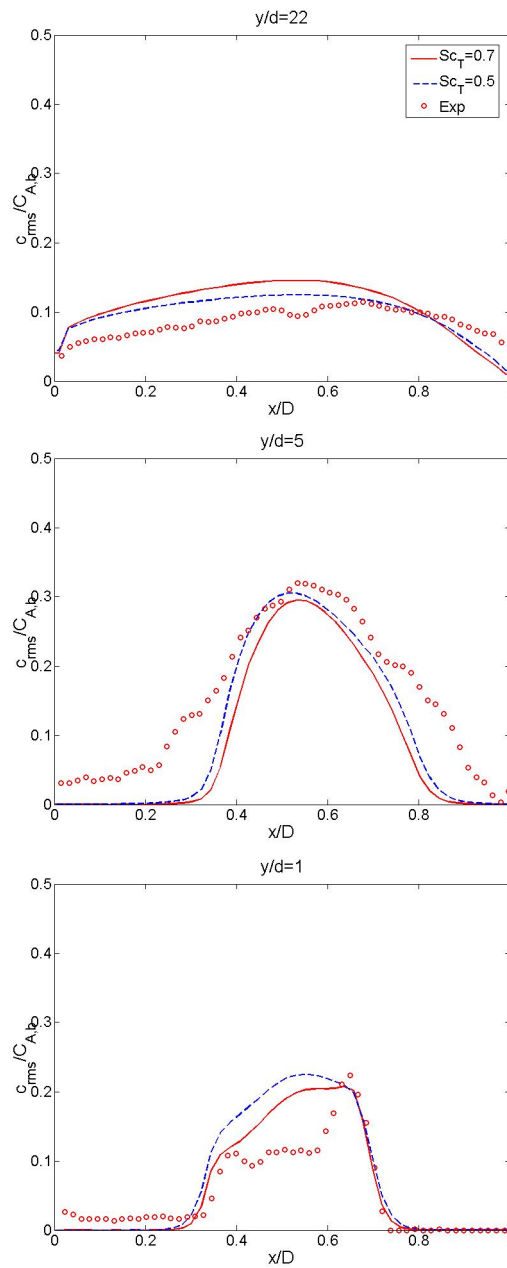
**Figure 10.** Continued.

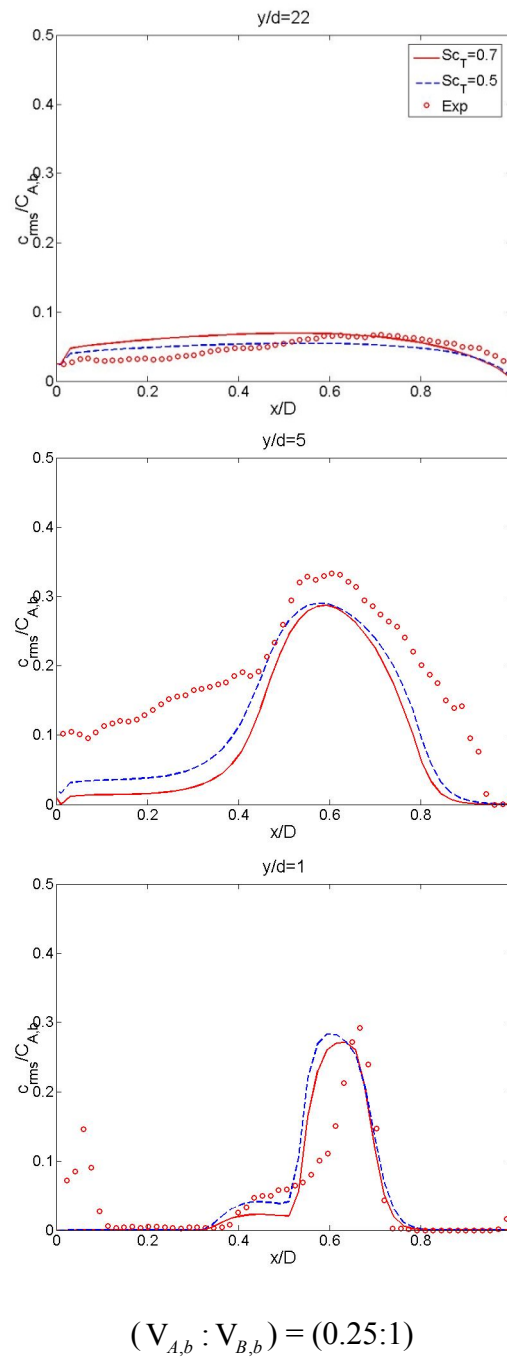$$( V_{A,b} : V_{B,b} ) = (0.25{:}1)$$

**Figure 10.** Measured and predicted concentration fluctuations for the three flow cases.

He et al. (1999) have tested the adequacy and accuracy of the constant turbulent Schmidt number assumption in predicting turbulent scalar fields in jet-in-cross-flows. They have simulated a round jet that was injected into a confined cross-flow in a rectangular tunnel using the RANS equations with the standard $k - \varepsilon$ turbulence model. The major observation in their work is that the turbulent Schmidt number has a significant effect on the prediction of the species spreading rate in jet-to-cross flows, especially for the cases where jet-to-cross flow momentum flux ratios are relatively small. They recommended a turbulent Schmidt number of 0.2 for best agreement with experimental data, which is close to 0.15 found for case 1 in this work.

Pollei et al. (2000) have studied a simple mixing tube where the inlet cross section was divided into two coaxial regions where the reactants entered. They measured the mixing length visually and compared it with numerical simulations. The mixing predicted with a Schmidt number of 0.9 was too strong. The predicted mixing length was 2/3 of the measured one. They obtained a very good agreement between experiments and simulations for a Schmidt number of 2.5. In the case studied here and in the work of He et al. (1999) the turbulent Schmidt number had to be reduced to fit the experimental results. This indicates that the turbulent Schmidt number may be flow dependent and that there may be introduced a significant uncertainty by using a constant value.

## 4.4 Analysis of degree of mixing

Mixing can be described as the process by which a non-uniform system is made uniform. The degree of mixing, or the uniformity, can be analysed by evaluating how well the flow is macro- or micromixed. Macromixing means that there is no mixing on molecular scale, but fluid elements are well mixed on a large scale. Micromixing is complete mixing of species on molecular scale. A measure of uniformity is the Coefficient of Variation, $CoV$, which is the ratio of the standard deviation in concentration and the cross-sectional average of concentration (Bakker et al., 1998). The coefficient of variation may be viewed as a measure of the macromixing. When the flow is totally unmixed the $CoV = 1$, and when it is fully mixed it reaches a value of $CoV = 0$.

To analyse the degree of micromixing another quantity called the decay function is evaluated. The decay function, $d$, can be expressed as the ratio between the cross-sectional average of the concentration fluctuations and the cross-sectional average of the concentration (Bird et al., 2002). The decay function starts at a value of $d = 0$, when the flow is totally unmixed, increases to a certain peak value and decreases again and reaches $d = 0$ when the flow is fully micromixed.

In Figure 11, the predicted and measured coefficient of variation ($CoV$) and decay function ($d$) are plotted along the channel length for all three flow cases. A cubic interpolation is made to give an impression of the curves in the region where experimental data are not available.

In the measurements, the coefficient of variation starts at a value of $CoV = 1$ at $y/d = 0$, where the two inlet streams are totally unmixed. Just after the block dividing the two inlet streams, the coefficient of variation drops suddenly to a value of about 0.85 for case 1, 0.75 for case 2 and 0.7 for case 3. This indicates that the flow in the recirculation zone is well macromixed. Further downstream, the coefficient of variation decreases steadily along the length of the channel as the velocity and concentration defects of the wake recover. At the last measurement point, the coefficient of variation is equal to a value of about 0.15 for case 1, 0.35 for case 2 and 0.50 for case 3. A coefficient of variation of 5% or less ($CoV < 0.05$) is considered to be satisfactory for most industrial blending operations (Bakker et al., 1998).

The decay function is closely related to the concentration fluctuations. Accordingly, the decay function starts at $d = 0$ at $y/d = 0$, where the two inlet streams are totally unmixed and there are no concentration fluctuations. In the near wake, the decay function increase rapidly to a maximum with increasing concentration fluctuations. Further downstream, the decay function decreases as the concentration defects recover and the concentration fluctuations decay in the far wake. At the last measurement point, the decay function is somewhat larger than the coefficient of variation indicating that the flow is better macromixed than micromixed.

When the predictions are compared with the measurements, the model defects discussed previously for the velocity and concentration predictions are reflected in the coefficient of variation and the decay function. As the recovery of the concentration defects are predicted to be too slow, the coefficient of variation is predicted to be larger than measured in the near wake. Consistently, the predictions are not as good macromixed as the measurements in the near wake. As the $k - \varepsilon$ turbulence models are unable to capture the large scale turbulence, the predicted mixing layers in the near wake are noted to have lower levels of concentration fluctuations and to be narrowere than measured. Accordingly, the decay function is predicted to be smaller than measured in the near wake suggesting better micromixing in the predictions than in the measurements. Except for case 3, where severe backflow occurred along the left channel wall, the predicted coefficient of variation and the decay function fit the experimental data quite well towards the end of the mixing channel.
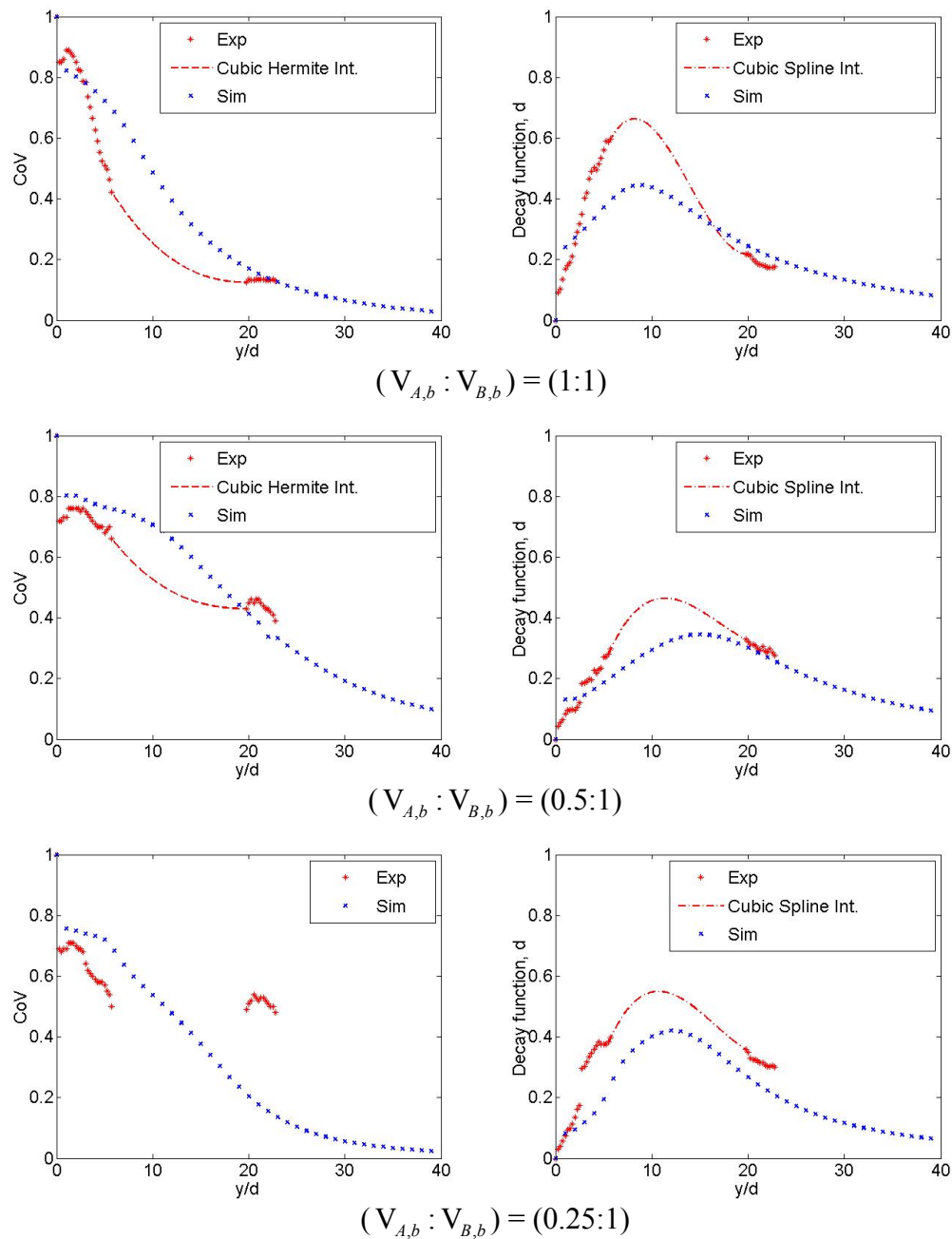
$$(V_{A,b} : V_{B,b}) = (1:1)$$



$$(V_{A,b} : V_{B,b}) = (0.5:1)$$



$$(V_{A,b} : V_{B,b}) = (0.25:1)$$

**Figure 11.** Predicted and measured coefficient of variation (left) and decay function (right) for the three flow cases.

## 4.5 Probability density functions (PDF)

The probability density function $P(\xi)$ is a measure of the probability of a certain mixture fraction $\xi$ to occur in a particular position in the flow. Figures 12 to 14 display predicted and measured PDF's at different positions in the mixing channel for the three flow cases.

The symmetric flow case, i.e. case 1, is shown in Figure 12. Along $x/D = 0.2$, which is close to the centreline of feed channel A (left feed channel), the PDF is represented by a single peak at $\xi = 1$ at the beginning of the mixing channel, where the two streams are unmixed. As the two streams mix, the PDF becomes a peak with a tail towards the smaller mixture fractions. At the end of the mixing channel, where the two streams are fairly well mixed, the PDF becomes ball-shaped with a mean mixture fraction approaching $\xi = 0.5$ from above. A similar behaviour is seen along $x/D = 0.8$, which is close to the centreline of feed channel B (right feed channel). At the beginning of the mixing channel, the PDF is represented by a single peak at $\xi = 0$. As the two streams mix, the PDF becomes a peak with a tail towards the larger mixture fractions. At the end of the mixing channel, the PDF becomes bell-shaped with a mean mixture fraction approaching $\xi = 0.5$ from below. Along $x/D = 0.5$, which is the centreline of the mixing channel, the PDF is bell-shaped with a mean mixture fraction around $\xi = 0.5$ at the beginning and at the end of the mixing channel where the two streams are fairly well mixed. In between, the PDF is more flat with two smaller peaks at both ends.

In the predictions, the PDF is represented by the volume fraction $p_n$ and the mean mixture fraction $\langle \xi \rangle_n = \langle s_\xi \rangle_n / p_n$ for each peak or environment. Accordingly, the PDF is calculated from the transport equations for volume fraction $p_n$ and volume-weighted mixture fraction $\langle s_\xi \rangle_n$ given by Eqs. (13) and (16). These transport equations depend strongly on the calculation of the mean and fluctuating velocity fields. A particularly important parameter is the rate of micromixing which is the inverse of the micromixing timescale. Generally, the predictions of the PDF's agree reasonably well with the measurements. Along the centreline of the mixing channel, the predictions appear to be better mixed in the near wake than that observed in the measurements. Here, the micromixing timescale is predicted too short because the turbulence level is predicted too low. Accordingly the rate of micromixing is predicted too high. Along the centrelines of the two feed channels, the predictions appear to be poorer mixed in the near wake than that observed in the measurements. As the $k - \varepsilon$ turbulence models fail

# Five-peak presumed PDF model $(v_{A,b} : v_{B,b}) = (1:1)$



**Figure 12.** Predicted (arrows) and measured (bars) probability density functions at different axial and radial positions for case 1.

Five-peak presumed PDF model $(v_{A,b} : v_{B,b}) = (0.5:1)$
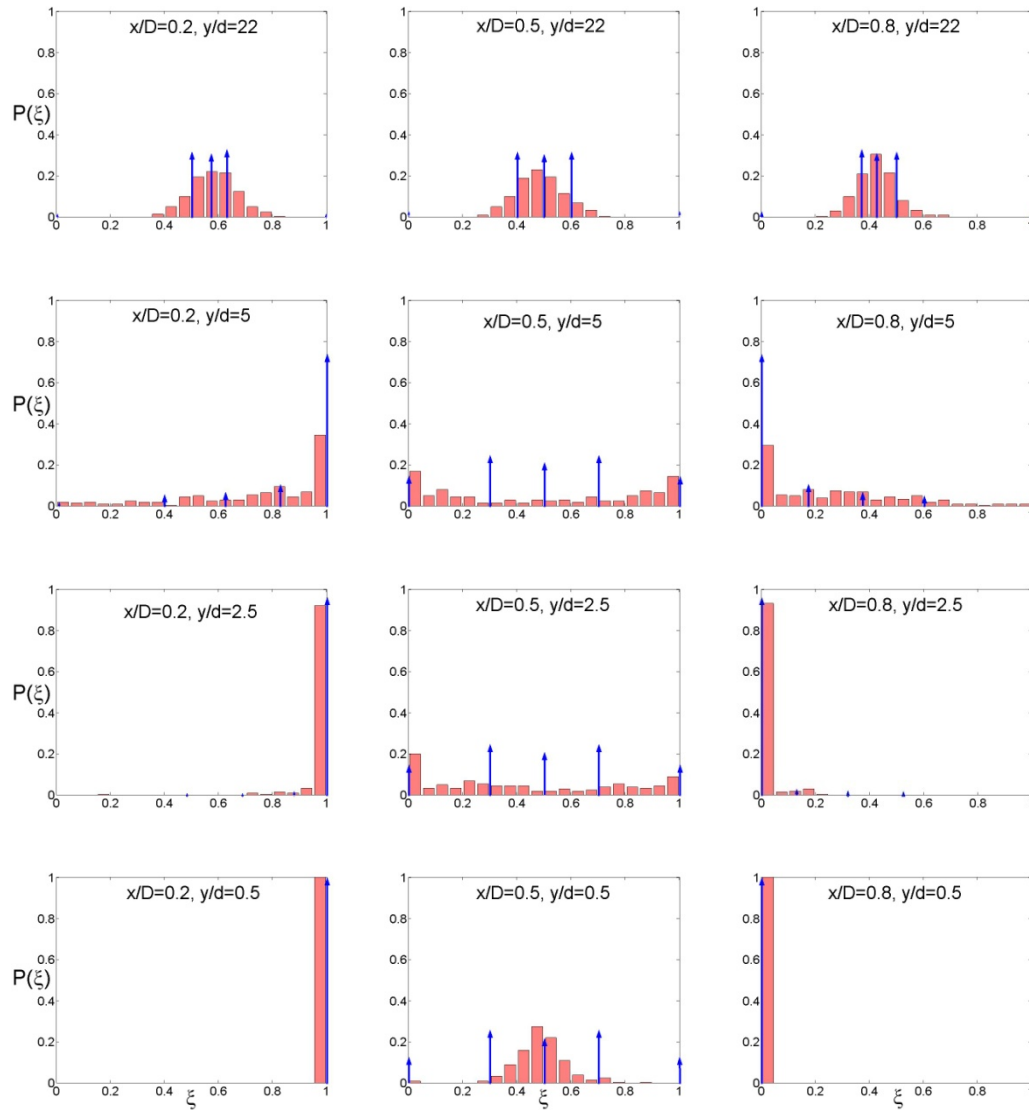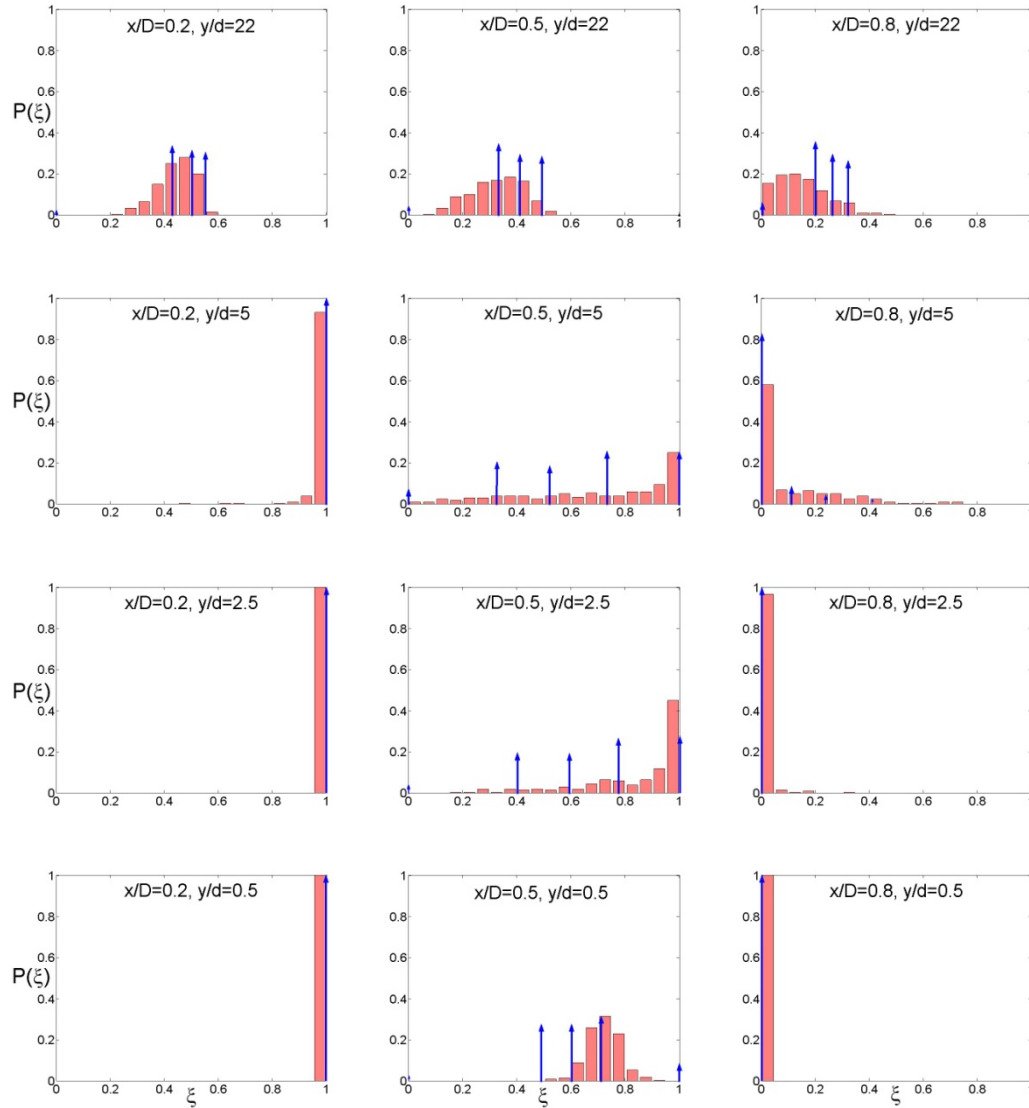


**Figure 13.** Predicted (arrows) and measured (bars) probability density functions at different axial and radial positions for case 2.

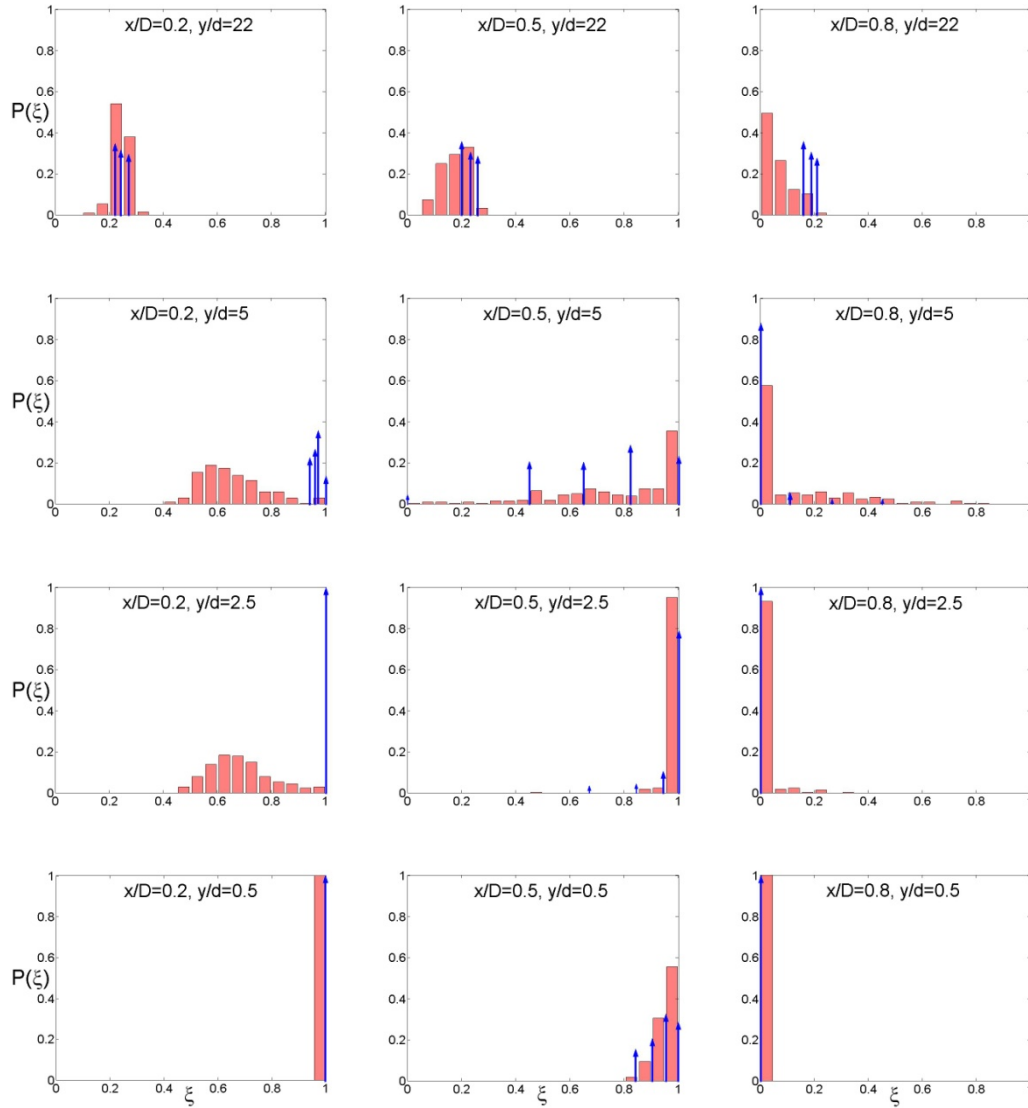# Five-peak presumed PDF model $(v_{A,b} : v_{B,b}) = (0.25:1)$



**Figure 14.** Predicted (arrows) and measured (bars) probability density functions at different axial and radial positions for case 3.

to capture the large scale turbulence, the recovery of the velocity defect and the growth of the wake shear layers are both too slow. Accordingly the rate of micromixing is predicted too low.

The asymmetric flow cases, i.e. case 2 and 3, where the wake is shifted towards the feed channel with the lower flow rate, are shown in the Figures 13 and 14. Compared with the symmetric flow case, the PDF's show less spreading over the mixture-fraction space. Besides, the PDF's are shifted towards the mixture fraction of the feed channel with the higher flow rate, i.e. $\xi = 0$. Apparently, the mixing becomes poorer by reducing the flow rate of one of the feed channels.

Again the predictions of the PDF's agree reasonably well with the measurements as long as severe backflow does not occur. The severe backflow observed experimentally in case 3 is not predicted by the $k - \varepsilon$ turbulence models.

## 5. CONCLUSIONS

Mass transfer in a turbulent liquid flow has been investigated both experimentally and numerically. A combined PIV/PLIF technique is used to measure instantaneous velocity and concentration fields. The steady turbulent flow is modelled in two-dimensions by solving the Reynolds-Averaged Navier-Stokes equations in combination with various forms of the $k - \varepsilon$ turbulence model. The multi-peak presumed PDF model using 5 peaks is used for calculation of the mass transfer process.

The different $k - \varepsilon$ turbulence models do not manage to capture the correct recovery from wake flow to channel flow, especially for the 1:1 case. The defects in the flow modelling are also seen in the mixing predictions. A reduction of the turbulent Schmidt number (0.15 for 1:1 case and 0.5-0.7 for the other two cases) is needed to achieve good predictions of both mean and rms. concentrations. The five-peak presumed PDF model predicts the stream wise decay of micromixing reasonably correct. The concentration PDF's as well as the coefficient of variation and the decay function are all reasonably well predicted.

A LES turbulence model is probably required to improve the flow and mass transfer modelling. Future solution of the multi-peak PDF model should use the direct quadrature method of moments (DQMOM) technique to account for the *spurious* dissipation rate in the mixture-fraction variance transport equation in a general way (Wang et al, 2004).

## NOMENCLATURE

| | |
|---|---|
| $C$ | local mean concentration [-] |
| $CoV$ | coefficient of variation [-] |
| $D$ | channel width [m] |
| $d$ | block width [m] or decay function [-] |
| $f_\phi$ | probability density function [-] |
| $G_n(p)$ | probability exchange rate between peaks or environments [1/s] |
| $I$ | local fluorescence intensity [-] |
| $J_{\phi,j}$ | turbulent Reynolds scalar flux vector [kg/m$^2$ s] |
| $k$ | turbulent kinetic energy [m$^2$/s$^2$] |
| $M_\xi^n(p,s)$ | scalar flux between peaks or environments [1/s] |
| $N_e$ | total number of environments [-] |
| $N_s$ | total number of scalars [-] |
| $n$ | peak or environment number [-] |
| $P$ | mean pressure [N/m$^2$] |
| $P_k$ | production of turbulent kinetic energy [kg/m s$^3$] |
| $P(\xi)$ | probability density function [-] |
| $p_n$ | probability/volume fraction of peak or environment $n$ [-] |
| $r_n$ | probability flux [-] |
| $S$ | mean strain rate [1/s] |
| $S_{ij}$ | mean rate of strain tensor [1/s] |
| $Sc$ | Schmidt number [-] |
| $\langle s_\xi \rangle_n$ | volume-weighted mixture fraction in peak or environment $n$ [-] |
| $t$ | time [s] |
| $U$ | mean transverse velocity [m/s] |
| $U_i$ | mean velocity in $i$-direction [m/s] |
| $u_i'$ | fluctuating velocity in $i$-direction [m/s] |
| $V$ | mean axial velocity or bulk velocity [m/s] |
| $x$ | transverse coordinate direction [m] |
| $x_i$ | coordinate in $i$ − direction [m] |
| $y$ | axial direction [m] |

Greek letters

| | |
|---|---|
| $\delta$ | Dirac delta function |
| $\delta_{ij}$ | Kronecker delta |
| $\varepsilon$ | dissipation of turbulent kinetic energy $[\text{m}^2/\text{s}^3]$ |
| $\phi$ | mean scalar variable $[-]$ |
| $\phi'$ | fluctuating scalar variable $[-]$ |
| $\langle \phi_\alpha \rangle_n$ | mean concentration of scalar $\alpha$ in peak or environment $n$ $[-]$ |
| $\gamma$ | rate of micromixing $[1/\text{s}]$ |
| $\Gamma_\phi$ | turbulent transport coefficient of scalar $\phi$ $[\text{kg/m s}]$ |
| $\eta$ | timescale ratio between the turbulence and mean flow $[-]$ |
| $\mu_T$ | turbulent viscosity $[\text{kg/m s}]$ |
| $\rho$ | density $[\text{kg/m}^3]$ |
| $\sigma_\phi$ | turbulent Prandtl/Schmidt number for variable $\phi$ $[-]$ |
| $\tau_m$ | characteristic timescale for micro-mixing $[\text{s}]$ |
| $\tau_{ij}$ | turbulent Reynolds stress tensor $[\text{kg/m s}^2]$ |
| $\xi$ | mixture fraction $[-]$ |
| $\langle \xi \rangle_n$ | local mixture fraction in peak or environment $n$ $[-]$ |
| $\langle \xi \rangle$ | mean mixture fraction $[-]$ |
| $\langle \xi'^2 \rangle$ | mixture-fraction variance $[-]$ |
| $\psi_\alpha$ | concentration space coordinate of scalar $\alpha$ $[-]$ |

Subscripts

| | |
|---|---|
| $A$ | feed channel A |
| $B$ | feed channel B |
| $b$ | bulk |
| $back$ | background |
| $e$ | environment |
| $k$ | turbulent kinetic energy |
| $m$ | micromixing |
| $n$ | peak or environment number |
| $ref$ | reference |
| $rms$ | root mean square |
| $s$ | scalar |
| $T$ | turbulent |

| $\alpha$ | scalar number |
|---|---|
| $\phi$ | scalar variable |
| $\xi$ | mixture fraction |

## REFERENCES

Aanen, L., Telesca, A. and Westerweel, J. (1999). "Measurement of turbulent mixing using PIV and LIF". Machine Graphics & Vision, Vol. 8, 529-543.

Bakker, A., LaRoche, R. D. and Marshall, E.M. (1998). "Laminar flow in static mixers with helical elements". The online CFM Book. Available at: http://www.bakker.org/cfm.

Bird, R.B., Stewart, W. E. and Lightfoot, E. N. (2002). "Transport phenomena, $2^{nd}$ Edition". John Wiley & Sons, Inc..

Borg, A., Bolinder, J. and Fuchs, L. (2001). "Simultaneous velocity and concentration measurements in the near field of a turbulent low-pressure jet by digital particle image velocimetry-planar laser-induced fluorescence". Experiments in Fluids. Vol. 3, 140-152.

Feng, H., Olsen, M.G., Liu, Y., Fox, R.O. and Hill, J.C. (2005). "Investigation of turbulent mixing in a confined planar-jet reactor", AIChE Journal, Vol. 51, 2649-2664.

Fox, R.O. (1998). "On the relationship between Lagrangian micromixing models and computational fluid dynamics". Chemical Engineering and Processing, Vol. 37, 521-535.

Fukushima C., Aanen, L. and Westerweel, J. (2000). "Investigation of the mixing process in an axisymmetric turbulent jet using PIV and LIF". $10^{th}$ International Symposium on Application of Laser Techniques to Fluid Mechanics, 10-13 July, Lisbon, Portugal.

He, G., Guo Y. and Hsu, T. (1999). "The effect of Schmidt number on turbulent scalar mixing in a jet-in-crossflow". International Journal of Heat and Mass Transfer, Vol. 42, 3727-3738.

Hjertager, L.K, Hjertager, B.H, Deen, N.D. and Solberg, T. (2003). "Measurement of turbulent mixing in a confined wake flow using combined PIV and PLIF", Canadian Journal of Chemical Engineering, Vol. 81, 1149-1158.

Hjertager Osenbroch, L.K., Hjertager, B.H. and Solberg, T. (2005). "Experiments and CFD modelling of fast chemical reactions in turbulent liquid flows". International Journal of Chemical Reactor Engineering, Vol. 3: A55.

Hjertager Osenbroch, L.K. (2004). "Experimental and computational study of mixing and fast chemical reactions in turbulent liquid flows", Ph.D. - thesis, Aalborg University Esbjerg, Denmark. Available at: http://hugin.aue.auc.dk.

Law, A.W.-K. and Wang, H. (2000). "Measurement of mixing processes with combined digital particle image velocimetry and planar laser induced fluorescence". Experimental Thermal and Fluid Science, Vol. 22, 213-229.

Marchisio, D.L., Fox, R.O, Barresi, A.A. and Baldi, G. (2001). "On the comparison between presumed and full PDF methods for turbulent precipitation". Industrial & Engineering Chemistry Research, Vol. 40, 5132-5139.

Meyer, K. E., Özcan, O. and Larsen, P.S (2000). "Point and planar LIF for velocity-concentration correlations in a jet in cross flow". 10th International Symposium on Application of Laser Techniques to Fluid Mechanics, 10-13 July, Lisbon, Portugal.

Piton, D., Fox, R.O. and Marcant, B. (2000). "Simulation of fine particle formation by precipitation using Computational Fluid Dynamics". Canadian Journal of Chemical Engineering, Vol. 78, 983-993.

Pollei, A., Borowski, T. and Kraume, M. (2000). "Simulation of Turbulent Mixing in precipitation Reactors". In the 14th International Congress of Chemical and Process Engineering, 27-30 August, Praha, Czech Republic.

Schmalzriedt, S., Jenne, M., Mauch, K. and Reuss, M. (2003). "Integration of physiology and fluid dynamics". Advances in Biochemical Engineering, Biotechnology, Vol. 80, 19-68.

Tsai, K., Larkins, R., Spradling, R., Sen, S. Lipp, C., Gillis, P. and Melton, L. (1999). "Development of a simultanous PIV/Reactive PLIF system for turbulent liquid flows". In the AIChE Annual Meeting, 31 October – 5 November, Dallas, TX, USA.

Versteeg, H.K. and Malalasekera, W. (1996). "An introduction to computational fluid dynamics. The finite volume method". Addison Wesley Longman Limited.

Wang, L. and Fox, R.O. (2004). "Comparison of micromixing models for CFD Simulation of nanoparticle formation", AIChE Journal, Vol. 50, 2217-2232.